A Numerical Study of Shock-Induced Cavity Collapse

M. Ozlem · **D.W. Schwendeman** · **A.K. Kapila** · **W.D. Henshaw**

Abstract The flow field resulting from the interaction between a planar incident shock in a solid and an embedded ellipsoidal gas cavity is examined computationally. The study is motivated by the need for improved understanding of the role of embedded cavities in the initiation of reaction in a heterogeneous explosive following the application of a shock. The system is modeled as a compressible multi-fluid flow with a sufficiently strong shock in the solid. A high-resolution, Godunov-type capturing scheme is employed to solve the governing equations numerically. The calculations are performed in parallel and use adaptive mesh refinement to obtain well-resolved solutions. The goal is to identify regions in which the shock-cavity interaction results in pressures that are substantially higher than the post-shock pressure that existed prior to the beginning of the interaction. Also of interest are the ways in which the magnitude of the elevated pressure, the extent and location of the regions where it develops, and the mechanisms that underlie such a development are influenced by the strength of the shock and the geometry of the cavity.

M. Ozlem
Department of Mathematical Sciences
Rensselaer Polytechnic Institute, Troy NY 12180
E-mail: ozlemm@rpi.edu

D.W. Schwendeman
Department of Mathematical Sciences
Rensselaer Polytechnic Institute, Troy NY 12180
E-mail: schwed@rpi.edu

A.K. Kapila
Department of Mathematical Sciences
Rensselaer Polytechnic Institute, Troy NY 12180
E-mail: kapila@rpi.edu

W.D. Henshaw
Center for Applied Scientic Computing
Lawrence Livermore National Lab., Livermore CA 94551
E-mail: henshaw1@llnl.gov

1 Introduction

The problem considered in this paper concerns the shock-induced collapse of a gas-filled cavity embedded in a solid. Our interest in this problem is motivated by the need for an improved understanding of the role of embedded cavities in the initiation of reaction in a heterogeneous explosive following the application of a shock. A practical explosive is a complex mixture formed by grains of the reactive constituent held together by an inert plastic binder, and contains such inclusions as voids, gas-filled pores, and impurities of various kinds. Application of a shock leads to a nonuniform deposition of energy in the shocked material as a variety of grain-scale mechanical processes such as friction, compaction, local plastic deformation and cavity collapse come into play. The result is a correspondingly nonuniform post-shock state, and reaction is initiated preferentially at sites where the pressure and temperature rise to levels considerably above their values in the bulk. We shall concentrate specifically on computing the nonuniform flow field that develops subsequent to the impact of an incident shock on a single gas-filled cavity. Attention is focused on identifying regions of the flow in which the shock-cavity interaction results in pressures that are substantially higher than the post-shock pressure that exists prior to the beginning of the interaction. Also of interest are the ways in which the strength of the shock and the geometry of the cavity determine the magnitude of the elevated pressure, the extent and location of the regions where it develops, and the mechanisms that underlie such a development. The impetus behind our focus on pressure arises from the pressure sensitivity of reactions in condensed explosives. If temperature is the rate-determining

state variable, then it is a simple matter to address temperatures instead by appealing to thermal equations of state for the constituents.

Cavity collapse in the context of explosive ignition has been the subject of many previous investigations, largely experimental but some theoretical as well. The experimental work is well-summarized in the review by Bourne [7]. Also noteworthy are the experiments on cavity collapse in porous explosives carried out by Bourne and Field [8]. In these experiments, a circular cavity is punched in a planar sheet of gelatinous material or in a sheet of emulsion explosive, and is subject to a planar shock. Multiple cavities arranged in an array are also considered. The primary conclusion is that the incident shock induces convergent flow resulting in the formation of a high-speed jet, and the site of maximum temperature is behind the point of impact of the jet with the cavity wall. The authors note that other locations of elevated temperature may also arise as a result of complex hydrodynamic interactions generated by the incident shock, and that the size of the cavity plays an important role in determining the location of the ignition sites. Milne and Bourne [18] present numerical computations aimed at simulating the experiments discussed in [8]. No details of the numerical procedure are provided, other than the observation that the computations employ a multi-material Eulerian hydrocode. Figures demonstrating the final stages of the collapse of the cavity are presented, and show the formation of lobes subsequent to the jet impact. It is mentioned that temperatures attained during collapse are a strong function of the assumptions about the equations of state. Ball, Howell, Leighton and Schofield [4], also motivated by the explosive initiation problem, use a Lagrangian code to simulate the collapse of a cylindrical air cavity in water by an incident shock. The air-water interface is tracked throughout the calculation. Many details of shock/cavity interaction are identified, including those that experimentalists find difficult to observe or measure. It is pointed out that a conventional adiabatic approximation for the gas region where a spatially uniform isentropic compression model is used to determine the temperatures is inappropriate in this case, and underestimates the pressures and temperatures achieved. Instead, gas within the cavity is heated and compressed by a sequence of multiply reflected shock waves.

Shock-cavity interactions also figure prominently in many other engineering and scientific applications besides ignition of energetic materials. These include physics of fluid mixing in terrestrial and astrophysical flows [11,3], shock-wave lithotripsy treatment for the pulverization of kidney stones [15], inertial confinement fusion [27], enhancement of supersonic combustion [17], and deflagration-to-detonation transition following shock-flame interaction [16]. Most of these studies consider gaseous cavities within a gaseous bulk, but some consider the fluid in the outer region to be water. Both slow/fast (faster acoustic speed in the cavity) and fast/slow (faster acoustic speed in the bulk) cases have been considered. Prominent among these are the experimental observations of shock-induced deformation of gas-filled bubbles in air by Haas and Sturtevant [11]. These experiments are conducted on cylindrical and spherical bubbles, and observations consist of shadowgraphs and pressure measurements. In a related paper, Quirk and Karni [19] review previous numerical work relevant to these experiments, point to its shortcomings, and note in particular that the under-resolved nature of the previous studies renders them prone to misinterpretation. Guided by the experiments, they simulate both the slow/fast and the fast/slow cases. The two-component fluid is taken to be a binary mixture with a single velocity and pressure. Shocks are captured rather than tracked, and the equations governing the flow are written in the primitive-variable form, aided by higher-order correction terms to produce a nearly conservative scheme. The simulations reproduce quite well the principal features described in [11], and provide many details of the hydrodynamic interactions which the experiments were unable to capture.

The studies described above are examples of multi-fluid, or more generally multi-material, systems in which the components remain immiscible and interfaces retain their identities. Such systems have attracted substantial attention from computational scientists. In the compressible case, it is well known that classical finite volume schemes lead to spurious pressure oscillations at interfaces. In the context of interface-capturing methods, the issue has been addressed by a number of investigators using both primitive and conservative formulations of the governing equations. A prominent approach is due to Abgrall [1] who examined a uniform pressure and velocity (UPV) flow involving an interface and demonstrated that the aforementioned oscillations can be suppressed by a special discretization of the advection equation for the specific heats ratio. Later, Saurel and Abgrall [22] extended this approach by advecting certain other constituent properties in a similar vein, and Jenny *et al.* [14] devised an energy correction for the same purpose. In recent work, a similar approach involving an energy correction was employed by Banks *et al.* [5,6] to study multi-material systems with more general equations of state suitable for the study of detonation diffraction with compliant confinement. An overview of numerical methods for multi-material problems, including methods based on interface tracking, is provided in [2].

In the present work our interest is in shocks that are strong enough so that the post-shock pressure in the solid is higher than its yield strength. The dominant forces responsible for the motion of the interface are the inertia of the solid and the pressure gradient, and it is expected that surface tension will play a negligible role. Because of the very short

time scales involved during the process of collapse, viscosity and heat conduction are omitted. This leads us to consider an idealized model under the assumption that the bulk solid and the gaseous content of the cavity are both compressible, inviscid fluids, here treated as stiffened gases but with different constitutive characteristics. Even though this study is motivated by explosive ignition, we do not model a particular experiment or a specific material. Our computational framework can accommodate a broad range of constitutive behavior, and the idealized models chosen here should be viewed as illustrative. Thus the stiffened-gas equation of state can easily be replaced by more realistic choices such as Mie-Grüneisen or Jones-Wilkins-Lee, for example [10]. We confine attention to the inert problem as the intent is to identify regions of the flow where the local state is apt to become a site of reaction initiation, rather than achieve a description of propagating combustion caused by reaction spreading into the bulk. In contrast to previous work, we consider the more general case in which the cavity is an ellipsoid rather than a sphere, but stress that yet more general shapes can also be accommodated using our numerical approach. Finally, we consider an entirely new fast/slow regime in which the bulk material and the cavity have vastly disparate acoustic impedances.

The resulting system of equations is an extension of the Euler equations of gasdynamics. Accurately capturing the sharp interface between the solid and the gas with a large jump in the acoustic impedance is the primary numerical challenge. Our approach assumes that the interface has a finite thickness, extending to a few computational cells, in which both the solid and the gas coexist simultaneously in the form of a mixture. In fact, we extend the notion of the mixture to the entire computational domain, with the understanding that one or the other of the two constituents is essentially absent in the bulk of the domain, with the exception of the thin interfacial zone. Given the equations of state of the individual components, construction of the equation of state of the mixture, in general, requires some assumptions about mutual interaction between the constituents, such as exchange of momentum and energy. These are the so-called closure conditions for the mixture. We take the position that since the mixture is introduced purely as a numerical construct designed to facilitate the treatment of the interface, we are afforded a greater latitude in the selection of closure conditions. In particular, we base our choice on considerations of computational convenience and robustness rather than on any preconceived physics of the interface. Our mathematical formulation assumes that certain constitutive parameters advect with the mixture, which follows similar formulations used by others (see [22], for example). The numerical approach used to compute solutions of the governing equations is a high-resolution Godunov scheme similar to that described by Schwendeman *et al.* [24,23] for the equations modeling two-phase reactive flow. The approach employs the exact solution of a Riemann problem to compute numerical fluxes and to advance the constitutive parameters which determine the state of the mixture and are governed by non-conservative advection equations. The choice of the numerical discretization is not guided by the constraint of preserving UPV flow directly, but rather this property holds as a consequence of the numerical approach as we discuss in more detail below.

The subsequent sections of the paper begin with a discussion of the governing equations and the physical setup in Section 2. The numerical method used to compute solutions of the equations is described in Section 3, and the results of various test problems are given in Section 4 to verify the accuracy and convergence properties of the scheme. Section 5 contains a detailed description of shock-induced cavity collapse for four configurations involving incident shocks of two different strengths and gas-filled cavities of three different shapes. Conclusions of our numerical study are provided in Section 6.

2 Governing equations

We consider a multi-material flow consisting of a gas-filled cavity surrounded by a solid. An incident planar shock propagates in the solid towards the cavity. The jump in the pressure across the shock is assumed to be large so that the motion of the solid in the disturbed region behind the shock is modeled as a compressible fluid with a suitable equation of state. In two space dimensions, the equations are

$$\frac{\partial}{\partial t}\mathbf{u} + \frac{\partial}{\partial x}\mathbf{f} + \frac{\partial}{\partial y}\mathbf{g} = 0 \,. \tag{1}$$

where

$$\mathbf{u} = \begin{bmatrix} \rho \\ \rho u \\ \rho v \\ \rho E \end{bmatrix}, \ \mathbf{f} = \begin{bmatrix} \rho u \\ \rho u^2 + p \\ \rho uv \\ u(\rho E + p) \end{bmatrix}, \ \mathbf{g} = \begin{bmatrix} \rho v \\ \rho uv \\ \rho v^2 + p \\ v(\rho E + p) \end{bmatrix}.$$

Here, ρ, (u,v), p, and E denote the density, velocity, pressure and total energy of the mixture, respectively, at a position (x,y) and time t. The total energy is given by

$$E = e + \frac{1}{2}\left(u^2 + v^2\right),$$

where the internal energy, e, is given by an equation of state of the mixture. For the present work, we assume a stiffened-gas equation of state for both constituents of the form

$$e = \frac{p + \gamma \pi}{(\gamma - 1)\rho} \,,$$

where γ is the ratio of specific heats and π is the stiffening pressure. The values for γ and π depend on the state of the mixture, and these advect with the multi-material flow which

is assumed to have a single velocity for both constituents. Following the formulations in [1] and [22], we consider the advection equation

$$\frac{\partial}{\partial t}\mathbf{w} + u\frac{\partial}{\partial x}\mathbf{w} + v\frac{\partial}{\partial y}\mathbf{w} = 0, \qquad (2)$$

where the two components of $\mathbf{w}$ are chosen to be

$$w_1 = \frac{1}{\gamma - 1}, \quad w_2 = \frac{\gamma\pi}{\gamma - 1}.$$

In this formulation, the state of the mixture is determined by $\mathbf{u}(x,y,t)$ and $\mathbf{w}(x,y,t)$, and the equation of state for the mixture is given by

$$e(\rho, p, w_1, w_2) = \frac{w_1 p + w_2}{\rho}. \qquad (3)$$

The governing equations for the flow are thus given by (1) and (2) with the mixture equation of state in (3).

The Euler equations in (1) are written in terms of the Cartesian coordinates (x, y). For the case of axisymmetric flow, we re-interpret x as the axial coordinate and y as the radial coordinate, and append the geometric source term

$$\mathbf{h} = -\frac{v}{y}\begin{bmatrix} \rho \\ \rho u \\ \rho v \\ \rho E + p \end{bmatrix},$$

to the right-hand side of (1). In this context u and v are the components of velocity in the axial and radial directions, respectively.

Figure 1 provides an illustration of the initial state of the flow. It is assumed that there is a planar shock with Mach number M_s traveling to the right into the undisturbed solid at rest in region Ω_s. The density and pressure of the solid in this region are given by ρ_s and p_s, respectively. The state of the solid in the region $\tilde{\Omega}_s$ behind the shock is determined by the normal shock conditions, i.e.

$$\frac{\tilde{\rho}_s}{\rho_s} = \frac{(\gamma_s + 1)M_s^2}{(\gamma_s - 1)M_s^2 + 2}, \quad \frac{\tilde{u}_s}{c_s} = \frac{2(M_s^2 - 1)}{(\gamma_s + 1)M_s},$$

$$\frac{\tilde{p}_s - p_s}{p_s + \pi_s} = \frac{2\gamma_s(M_s^2 - 1)}{\gamma_s + 1}, \qquad\qquad (4)$$

where γ_s and π_s are the ratio of specific heats and the stiffening pressure for the solid material, and c_s is the sound speed in the undisturbed solid. The initial state of the gas inside the cavity (region Ω_g) is taken to be at rest with density and pressure given by ρ_g and p_g, respectively. The ratio of specific heats and the stiffening pressure for the gas are given by γ_g and π_g, with the latter quantity taken to be zero. Finally, it is assumed that the gas inside the cavity and the solid surrounding it are in mechanical and thermal equilibrium across the interface Γ, a contact discontinuity, that forms the boundary of the cavity at $t = 0$.

We note that there is no region involving a mixture of gas and solid for the initial state described in Figure 1, and a
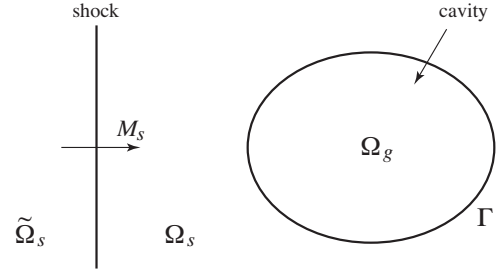

Fig. 1 Initial configuration for shock-induced cavity collapse. Regions Ω_g, Ω_s and $\tilde{\Omega}_s$ denote the gas in the cavity, the solid ahead of the shock and the solid behind the shock, respectively. The Mach number of the incident planar shock is given by M_s, and Γ denotes the boundary of the cavity.

mixture region would never develop in the exact solution of the flow at a later time. However, in our numerical approximation of the flow the interface is smeared initially over two or three grid cells, and the width of this smeared interface can increase as the solution evolves according to our shock-capturing scheme. The smeared interface involves a mixture, and thus we require a formulation of the governing equations which can handle a mixture. Such a formulation is described above and is well suited for our numerical scheme (see Section 3). For the calculations discussed later, the mixture regions are thin and purely numerical, and we assign no particular physical significance to the behavior of the flow variables in such regions.

The motivating application for the configuration in Figure 1 is shock-induced cavity collapse within a solid explosive. For this application, we take

$$\rho_g = 1.161 \text{ kg/m}^3, \quad p_g = 10^5 \text{ Pa},$$

$$\rho_s = 1905. \text{ kg/m}^3, \quad p_s = 10^5 \text{ Pa}.$$

These values are consistent with an air-filled cavity and a typical HMX-type explosive solid at standard atmospheric pressure and temperature. The parameters for the equations of state of the component materials are taken to be

$$\gamma_g = 1.4, \quad \pi_g = 0,$$

$$\gamma_s = 5.0, \quad \pi_s = 6.858 \times 10^8 \text{ Pa}.$$

From these parameters, we compute the sound speeds of the gas and solid in the undisturbed regions to be

$$c_g = \sqrt{\gamma_g p_g / \rho_g} = 347.2 \text{ m/s},$$

$$c_s = \sqrt{\gamma_s(p_s + \pi_s)/\rho_s} = 1342. \text{ m/s},$$

respectively. The initial state of the flow behind the shock is determined by the shock Mach number and the jump conditions in (4). For the calculations presented in this paper, we consider two values for the shock Mach number. For the weaker of the two cases, we assume $M_s = 1.2$ so that the speed of the shock in the solid is

$$D_s = c_s M_s = 1610. \text{ m/s},$$

Table 1 Dimensionless initial states in the undisturbed gas, Ω_g, and solid, Ω_s, and in the post-shock solid for $M_s = 1.2$, $\tilde{\Omega}_{s,\text{weak}}$, and for $M_s = 2.0$, $\tilde{\Omega}_{s,\text{strong}}$.

	Ω_g	Ω_s	$\tilde{\Omega}_{s,\text{weak}}$	$\tilde{\Omega}_{s,\text{strong}}$
ρ	1.4	2297.	2557.	3063.
u	0	0	0.4723	1.932
p	1.0	1.0	5031.	34300.
w_1	2.5	0.25	0.25	0.25
w_2	0	8572.	8572.	8572.

and the density, normal velocity, and pressure in region $\tilde{\Omega}_s$ are

$$\tilde{\rho}_s = 2121.\,\text{kg/m}^3, \quad \tilde{u}_s = 164.0\,\text{m/s},$$

$$\tilde{p}_s = 5.031 \times 10^8\,\text{Pa},$$

respectively. The stronger case assumes that $M_s = 2.0$. For this case the speed of the shock in the solid is

$$D_s = c_s M_s = 2683.\,\text{m/s},$$

and

$$\tilde{\rho}_s = 2540.\,\text{kg/m}^3, \quad \tilde{u}_s = 670.9\,\text{m/s},$$

$$\tilde{p}_s = 3.430 \times 10^9\,\text{Pa}.$$

The governing equations are made dimensionless by choosing suitable reference scales for the problem. A length scale is chosen based on an estimate for the diameter of a cavity in a typical solid explosive. A reference scale for velocity is taken to be the acoustic speed in the undisturbed gas, and a reference scale for pressure is standard atmospheric pressure. Thus, we have

$$x_{\text{ref}} = 10^{-4}\,\text{m}, \quad u_{\text{ref}} = c_g = 347.2\,\text{m/s},$$

$$p_{\text{ref}} = p_g = 10^5\,\text{Pa},$$

and from these, we compute

$$t_{\text{ref}} = x_{\text{ref}}/u_{\text{ref}} = 2.880 \times 10^{-7}\,\text{s},$$

$$\rho_{\text{ref}} = p_{\text{ref}}/u_{\text{ref}}^2 = 0.8295\,\text{kg/m}^3.$$

We now define the dimensionless quantities $x' = x/x_{\text{ref}}$, $y' = y/x_{\text{ref}}$, $t' = t/t_{\text{ref}}$, $\rho' = \rho/\rho_{\text{ref}}$, etc., and a dimensionless stiffening pressure

$$\pi_s' = \pi_s/p_{\text{ref}} = 6857.,$$

to convert the governing equations to dimensionless ones. The resulting equations have the same form as the original ones, and so the equations in (1), (2) and (3) may be viewed as dimensionless (with the primes on all variables dropped for notational convenience). The dimensionless quantities in the three regions of the initial configuration in Figure 1 are collected in Table 1.

3 Numerical method

A numerical method is used to obtain well-resolved solutions of the governing equations for different strengths of the incident shock in the solid and for various cavity shapes. The approach is a high-resolution Godunov method in which shocks and contact discontinuities (including the interface between the gas and solid) are captured in the numerical solution. An exact Riemann solver is used to compute the (conservative) flux functions in the Godunov method and to advance the constitutive variables in (2) following the approach described in [24,23]. We have found that more accurate results for the cavity problems considered here are obtained using an exact Riemann solver in comparison to results obtained using an approximate Riemann solver, such as an HLLC solver [25], which requires less computational cost per time step. The choice of the constitutive variables in (2) and the discretization of these advection equations is often guided by the property that UPV flow is maintained, and this is done so that oscillations in the pressure near the interface are suppressed (see [22], for example). The numerical approach described here is not guided directly by this property, but rather UPV flow is maintained as a consequence of the numerical approximation as is described below. Finally, the numerical method discussed in this section is part of the Overture set of codes (see Acknowledgements), and is implemented in parallel using adaptive mesh refinement (AMR) following the work in [12] and [13].

The numerical solution of the cavity problem shown in Figure 1 is computed on a uniform grid with spacings Δx and Δy in the x and y directions, respectively. For this grid the Euler equations in (1) are approximated using the conservative scheme

$$\mathbf{U}_{i,j}^{n+1} = \mathbf{U}_{i,j}^n - \frac{\Delta t}{\Delta x}\left(\mathbf{F}_{i+1/2,j}^n - \mathbf{F}_{i-1/2,j}^n\right) \\ - \frac{\Delta t}{\Delta y}\left(\mathbf{G}_{i,j+1/2}^n - \mathbf{G}_{i,j-1/2}^n\right). \tag{5}$$

Here, $\mathbf{U}_{i,j}^n$ is an approximation for $\mathbf{u}(x,y,t)$ at a grid cell (x_i, y_j) and a time t_n, Δt is a time step (chosen to satisfy a CFL stability condition), and $\mathbf{F}$ and $\mathbf{G}$ are numerical fluxes. The advection equation in (2) is approximated using the upwind scheme

$$\mathbf{W}_{i,j}^{n+1} = \mathbf{W}_{i,j}^n - \frac{\Delta t}{\Delta x}\left(\mathbf{R}_{\ell,i+1/2,j}^n - \mathbf{R}_{r,i-1/2,j}^n\right) \\ - \frac{\Delta t}{\Delta y}\left(\mathbf{S}_{\ell,i,j+1/2}^n - \mathbf{S}_{r,i,j-1/2}^n\right), \tag{6}$$

where $\mathbf{W}_{i,j}^n$ is an approximation for $\mathbf{w}(x_i, y_j, t_n)$, and $\mathbf{R}_{\ell,r}$ and $\mathbf{S}_{\ell,r}$ are approximations for $u\Delta x(\partial \mathbf{w}/\partial x)$ and $v\Delta y(\partial \mathbf{w}/\partial y)$, respectively. The latter approximations are obtained by an integration of (2) over a grid cell following a similar approach developed in [24] for a model of compressible two-phase flow.

Values for $(\mathbf{F}, \mathbf{G})$ in (5) and $(\mathbf{R}_{\ell,r}, \mathbf{S}_{\ell,r})$ in (6) are computed using exact solutions of suitable Riemann problems. For example, $\mathbf{F}$ and $\mathbf{R}_{\ell,r}$ at $(x_{i-1/2}, y_j)$ are determined from the solution of the Riemann problem given by

$$\frac{\partial}{\partial t}\mathbf{u} + \frac{\partial}{\partial x}\mathbf{f} = 0, \quad \frac{\partial}{\partial t}\mathbf{w} + u\frac{\partial}{\partial x}\mathbf{w} = 0, \quad t > t_n,$$

with initial data

$$\mathbf{u}(x, t_n) = \begin{cases} \mathbf{u}_\ell & \text{if } x < x_{i-1/2}, \\ \mathbf{u}_r & \text{if } x > x_{i-1/2}, \end{cases}$$

$$\mathbf{w}(x, t_n) = \begin{cases} \mathbf{w}_\ell & \text{if } x < x_{i-1/2}, \\ \mathbf{w}_r & \text{if } x > x_{i-1/2}, \end{cases}$$

where the left and right states for $\mathbf{u}$ and $\mathbf{w}$ are obtained from grid values on either side of $x_{i-1/2}$. A representative solution of the Riemann problem is illustrated in Figure 2. The solution consists of a shock or rarefaction in the $u \pm c$ characteristic fields $C_\pm$ and the intermediate states $\mathbf{u}_1$ and $\mathbf{u}_2$ separated by a contact along the particle path P. The left and right values for $\mathbf{w}$ are constant across shocks and rarefactions as shown in the figure, but may jump at the contact. The solution of the Riemann problem is found iteratively as discussed in Toro [25]. Assuming the solution is known, we set

$$\mathbf{F}_{i-1/2,j}^n = \begin{cases} \mathbf{f}(\mathbf{u}^*, \mathbf{w}_r), & \text{if } u_c < 0, \\ \mathbf{f}(\mathbf{u}^*, \mathbf{w}_\ell), & \text{if } u_c > 0, \end{cases} \quad (7)$$

where $\mathbf{u}^* = \mathbf{u}^*(\mathbf{u}_\ell, \mathbf{u}_r, \mathbf{w}_\ell, \mathbf{w}_r)$ is the solution for $\mathbf{u}$ on $x = x_{i-1/2}$ for $t > t_n$, and u_c is the velocity of the contact. For the discretization of the advection equation, we set

$$\mathbf{R}_{\ell,i-1/2,j}^n = \begin{cases} u_c(\mathbf{w}_r - \mathbf{w}_\ell) & \text{if } u_c < 0, \\ 0 & \text{if } u_c > 0, \end{cases}$$

$$\mathbf{R}_{r,i-1/2,j}^n = \begin{cases} 0 & \text{if } u_c < 0, \\ -u_c(\mathbf{w}_r - \mathbf{w}_\ell) & \text{if } u_c > 0. \end{cases} \quad (8)$$

(See [24] for further details.) Similar formulas are obtained for $\mathbf{G}$ and $\mathbf{S}_{\ell,r}$ by considering the corresponding Riemann problem in the y direction.
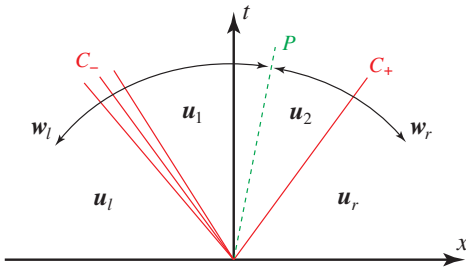

Fig. 2 Representative solution configuration for the Riemann problem. Left and right states are given by $(\mathbf{u}_\ell, \mathbf{w}_\ell)$ and $(\mathbf{u}_r, \mathbf{w}_r)$, respectively, and $\mathbf{u}_1$ and $\mathbf{u}_2$ are computed intermediate states.

If the left and right states for the Riemann problem are taken to be the cell values on either side of the cell boundary, then the discretizations in (5) and (6) are first-order accurate in space and time. For example, consider the UPV flow in which the velocity and pressure for all cells at $t = t_n$ are uniform and given by $(\bar{u}, \bar{v})$ and $\bar{p}$, respectively, with $\bar{u} > 0$ and $\bar{v} > 0$. For this case, there is no jump in $\mathbf{u}$ across the $C_\pm$ characteristic fields in Figure 2 so that

$$\mathbf{u}^* = \begin{bmatrix} \rho_\ell \\ \rho_\ell \bar{u} \\ \rho_\ell \bar{v} \\ w_{1,\ell} \bar{p} + w_{2,\ell} + \frac{1}{2}\rho_\ell \bar{q}^2 \end{bmatrix}, \quad \bar{q}^2 = \bar{u}^2 + \bar{v}^2,$$

for the solution of the Riemann problem in both the x and y directions. The Godunov fluxes in (5) are then computed using (7) with $u_c = \bar{u} > 0$ for $\mathbf{F}_{i\pm1/2,j}$ and a similar formula for $\mathbf{G}_{i,j\pm1/2}$ so that the first component in (5) is given by

$$\rho_{i,j}^{n+1} = \rho_{i,j}^n - \frac{\bar{u}\Delta t}{\Delta x}\left(\rho_{i,j}^n - \rho_{i-1,j}^n\right) \\ - \frac{\bar{v}\Delta t}{\Delta y}\left(\rho_{i,j}^n - \rho_{i,j-1}^n\right). \quad (9)$$

The second and third components in (5) with the upwind approximation in (9) give

$$\rho_{i,j}^{n+1} u_{i,j}^{n+1} = \rho_{i,j}^n \bar{u} - \frac{\bar{u}\Delta t}{\Delta x}\left(\rho_{i,j}^n \bar{u} - \rho_{i-1,j}^n \bar{u}\right) \\ - \frac{\bar{v}\Delta t}{\Delta y}\left(\rho_{i,j}^n \bar{u} - \rho_{i,j-1}^n \bar{u}\right) = \rho_{i,j}^{n+1} \bar{u},$$

$$\rho_{i,j}^{n+1} v_{i,j}^{n+1} = \rho_{i,j}^n \bar{v} - \frac{\bar{u}\Delta t}{\Delta x}\left(\rho_{i,j}^n \bar{v} - \rho_{i-1,j}^n \bar{v}\right) \\ - \frac{\bar{v}\Delta t}{\Delta y}\left(\rho_{i,j}^n \bar{v} - \rho_{i,j-1}^n \bar{v}\right) = \rho_{i,j}^{n+1} \bar{v},$$

which implies $u_{i,j}^{n+1} = \bar{u}$ and $v_{i,j}^{n+1} = \bar{v}$. Finally, the fourth component in (5) gives

$$\rho_{i,j}^{n+1} E_{i,j}^{n+1} = w_{1,i,j}^n \bar{p} + w_{2,i,j}^n + \frac{1}{2}\rho_{i,j}^n \bar{q}^2 \\ - \frac{\bar{u}\Delta t}{\Delta x}\left((w_{1,i,j}^n - w_{1,i-1,j}^n)\bar{p} \right. \\ + (w_{2,i,j}^n - w_{2,i-1,j}^n) \\ \left. + \frac{1}{2}(\rho_{i,j}^n - \rho_{i-1,j}^n)\bar{q}^2\right) \quad (10) \\ - \frac{\bar{v}\Delta t}{\Delta y}\left((w_{1,i,j}^n - w_{1,i,j-1}^n)\bar{p} \right. \\ + (w_{2,i,j}^n - w_{2,i,j-1}^n) \\ \left. + \frac{1}{2}(\rho_{i,j}^n - \rho_{i,j-1}^n)\bar{q}^2\right).$$

The upwind fluxes in (6) are computed using (8) for $\mathbf{R}_{\ell,r}$ and a similar formula for $\mathbf{S}_{\ell,r}$ to give

$$\mathbf{w}_{i,j}^{n+1} = \mathbf{w}_{i,j}^n - \frac{\bar{u}\Delta t}{\Delta x}\left(\mathbf{w}_{i,j}^n - \mathbf{w}_{i-1,j}^n\right) \\ - \frac{\bar{v}\Delta t}{\Delta y}\left(\mathbf{w}_{i,j}^n - \mathbf{w}_{i,j-1}^n\right). \quad (11)$$

The formulas in (9) and (11) can now be used in (10) to give

$$\rho_{i,j}^{n+1} E_{i,j}^{n+1} = w_{1,i,j}^{n+1} \bar{p} + w_{2,i,j}^{n+1} + \tfrac{1}{2} \rho_{i,j}^{n+1} \bar{q}^2$$

which implies $p_{i,j}^{n+1} = \bar{p}$. Thus, ρ and $\mathbf{w}$ evolve according to the first-order upwind approximations in (9) and (11), respectively, and (u, v) and p remain uniform for the UPV flow.

The discretizations in (5) and (6) become second-order accurate (for smooth flow) if slope-limited updates are used to obtain the left and right states for the Riemann problem. This is done by first writing the Euler equations in (1) in terms of the primitive variables (ρ, u, v, p), and combining them with the advection equations in (2). The governing equations, now in quasi-linear form, are then used to obtain first-order approximations for the states on either side of cell boundaries. The slope-limiting in these approximations is done in characteristic variables using a minimum-modulus limiter so that numerical oscillations about shocks and contacts are suppressed. Since the updates to the left and right states for the Riemann problem are done in primitive variables, the second-order scheme also maintains UPV flow. The full details of this approach are not given here, but they may be found in our previous work in [24] and [23], for example.

The numerical approach for multi-material flow as described above is performed in parallel using AMR. A uniform grid at the base level covers the domain of interest, and block-structured refinement grids are built on top of this uniform grid according to an error estimator so that sharp features of the flow, such as shocks and contact discontinuities (including the interface), are computed on the finest grid level (see [12] for further details). The grid cells are refined by a factor of $n_r = 4$ in each coordinate direction and n_ℓ refinement grid levels are allowed in the AMR hierarchy. Typically, we use $n_\ell = 1$ or 2. All grids, including the base-level grid and its refinement grids, may be partitioned and assigned to a set of processors, so that the calculations are done in parallel. The assignment is made according to a load-balancing algorithm as described in [13]. We generally use 32 processors for the numerical calculations presented later in this paper.

4 Grid convergence

In this section, we use the numerical approach for a set of test calculations to demonstrate that solutions converge with second-order accuracy for smooth flow and to illustrate the accuracy of solutions for problems involving the interaction of a shock with a solid-gas interface.

4.1 Method of analytic solutions

The method of analytic solutions is a useful technique to check that a numerical method is implemented correctly and to verify that numerical solutions converge at the correct rate. The technique, used early on for fluid dynamics in [9], later became known as the method of manufactured solutions [20, 21]. The idea is to choose smooth functions, $\hat{\mathbf{u}}(x, y, t)$ and $\hat{\mathbf{w}}(x, y, t)$, and then set forcing functions, $\hat{\mathbf{h}}(x, y, t)$ and $\hat{\mathbf{k}}(x, y, t)$, to be

$$\hat{\mathbf{h}} = \frac{\partial}{\partial t} \hat{\mathbf{u}} + \frac{\partial}{\partial x} \mathbf{f}(\hat{\mathbf{u}}, \hat{\mathbf{w}}) + \frac{\partial}{\partial y} \mathbf{g}(\hat{\mathbf{u}}, \hat{\mathbf{w}}),$$

$$\hat{\mathbf{k}} = \frac{\partial}{\partial t} \hat{\mathbf{w}} + \hat{u} \frac{\partial}{\partial x} \hat{\mathbf{w}} + \hat{v} \frac{\partial}{\partial y} \hat{\mathbf{w}},$$

so that $\mathbf{u} = \hat{\mathbf{u}}(x, y, t)$ and $\mathbf{w} = \hat{\mathbf{w}}(x, y, t)$ are exact solutions of the governing equations in (1) and (2) with forcing functions $\hat{\mathbf{h}}$ and $\hat{\mathbf{k}}$, respectively, appended to the right-hand sides of the equations. Simple functions, such as polynomials, are typically chosen for $\hat{\mathbf{u}}$ and $\hat{\mathbf{w}}$. For example, we choose $\hat{\mathbf{u}}$ by setting its corresponding primitive variables to be second-degree polynomials of the form

$$\hat{\rho}(x, y, t) = \left(\sum_{n \leq 2} \hat{a}_{\rho,n} t^n \right) \left(\sum_{m+n \leq 2} \hat{b}_{\rho,m,n} x^m y^n \right),$$

and similar forms for $\hat{u}$, $\hat{v}$ and $\hat{\varphi} = \hat{p}/\hat{\rho}$. Likewise, we define $\hat{\mathbf{w}}$ by setting

$$\hat{w}_i(x, y, t) = \left(\sum_{n \leq 2} \hat{c}_{i,n} t^n \right) \left(\sum_{m+n \leq 2} \hat{d}_{i,m,n} x^m y^n \right),$$

for $i = 1$ and 2. Here, the coefficients $(\hat{a}, \hat{b}, \hat{c}, \hat{d})$ are constants to be chosen.

Calculations are performed using the second-order scheme described in Section 3, but with slope corrections computed using simple averages instead of the minimum-modulus limiter. The calculations use exact initial data given by $\hat{\mathbf{u}}(x, y, 0)$ and $\hat{\mathbf{w}}(x, y, 0)$, and use exact Dirichlet data on the boundaries of the domain $\Omega = \{ 0 \leq x \leq L, \, 0 \leq y \leq H \}$, where $L = 1$ and $H = 1/2$. The coefficients in the second-degree polynomials are chosen at random on $[-1, 1]$ except for

$$\hat{a}_{\rho,0} = \hat{a}_{\varphi,0} = \hat{c}_{1,0} = \hat{c}_{2,0} = 1,$$

$$\hat{b}_{\rho,0,0} = \hat{b}_{\varphi,0,0} = \hat{d}_{1,0,0} = \hat{d}_{2,0,0} = 4,$$

which are chosen to ensure that $\hat{\rho}$, $\hat{p}$, $\hat{w}_1$ and $\hat{w}_2$ are positive for $(x, y) \in \Omega$ and for $0 \leq t \leq t_{\text{final}} = 1/2$. Table 2 gives the maximum errors, $\mathscr{E}$, for the components of the solution at $t = t_{\text{final}}$. These are computed by comparing numerical solutions given by $\mathbf{U}_{i,j}^n$ and $\mathbf{W}_{i,j}^n$ with the exact solution given by $\hat{\mathbf{u}}(x_i, y_j, t_n)$ and $\hat{\mathbf{w}}(x_i, y_j, t_n)$ for grids with $\Delta x = \Delta y = h = 1/40$, $1/80$ and $1/160$. The convergence rates, σ, shown in the table are determined by a least-squares fit to the logarithm of the curve $\mathscr{E} = Ch^\sigma$ for each component. These values indicate that the numerical scheme is second-order accurate for the case of smooth flow.

Table 2 Maximum errors, $\mathcal{E}$, in the components of the solution at $t_{\text{final}} = 1/2$ for grids with $h = 1/40$, $1/80$ and $1/160$. The rates, σ, are least-squares fits to the curve $\mathcal{E} = Ch^{\sigma}$ for each component.

h	$\mathcal{E}_{\rho}$	$\mathcal{E}_u$	$\mathcal{E}_v$	$\mathcal{E}_{\varphi}$	$\mathcal{E}_{w_1}$	$\mathcal{E}_{w_2}$
0.025	4.34e−5	2.13e−5	2.86e−5	2.13e−5	1.32e−5	5.31e−6
0.0125	1.06e−5	5.21e−6	7.74e−6	5.49e−6	3.32e−6	1.36e−6
0.00625	2.60e−6	1.28e−6	1.98e−6	1.40e−6	8.26e−7	3.42e−7
rate, σ	2.03	2.03	1.93	1.97	2.00	1.98

4.2 Shock interaction with a planar cavity: normal incidence

We now consider a Riemann problem involving the interaction of a planar shock in the solid with a planar interface separating the solid and a gas-filled cavity. The left state for this problem is taken to be

$$\rho_{\ell} = 3063., \quad u_{\ell} = 1.932, \quad p_{\ell} = 34300.,$$

$$\gamma_{\ell} = 5, \quad \pi_{\ell} = 6857.,$$

whereas the right state is given by

$$\rho_r = 1.4, \quad u_r = 0, \quad p_r = 1,$$

$$\gamma_r = 1.4, \quad \pi_r = 0.$$

The left state corresponds to the post-shock state in the solid for a shock with $M_s = 2.0$, while the right state corresponds to the undisturbed state in the gas-filled cavity (see Table 1). Thus, the initial conditions for the Riemann problem model the local behavior of the flow illustrated in Figure 1 at the instant the shock meets the cavity. The exact solution for this problem may be computed iteratively and it consists of a rarefaction in the C_- characteristic field and a shock in the C_+ characteristic field (see Figure 2). The state of the solid behind the rarefaction is found to be

$$\rho_1 = 2142.2, \quad u_1 = 4.0254, \quad p_1 = 29.343,$$

$$\gamma_1 = 5, \quad \pi_1 = 6857.,$$

while the state of the gas behind the shock is found to be

$$\rho_2 = 7.0136, \quad u_2 = 4.0254, \quad p_2 = 29.343,$$

$$\gamma_2 = 1.4, \quad \pi_2 = 0.$$

Since the impedance mismatch at the solid-gas interface is large, the jump in the states across the rarefaction and shock is corresponding large. For example, the (transmitted) shock in the gas is very strong with a shock Mach number found to be $M_g = 5.0293$.

As a test of the numerical approach, we compute solutions of the Riemann problem for the case when the jump between the left and right states is located at $x = 0.5$ initially. Numerical solutions are computed for $0 \le x \le 1$ and $0 \le t \le t_{\text{final}} = 0.06$ using three different base grids, each with two levels of AMR. The effective grid spacings are

$h_{\text{eff}} = 1/4000$, $1/8000$ and $1/16000$. Figure 3 shows the density, velocity, pressure and ratio of specific heats at $t = t_{\text{final}}$ from the exact solution (black curves) and from the three numerical solutions (blue, green and red curves). All of the numerical solutions are well resolved on the scale of the plots so that there is essentially no visible difference between the curves. We also note that the shock in the gas is not visible in the plots of density and pressure due to the vertical scale required to show the behavior of these quantities in the solid, while the shock in the gas is seen clearly in the plot of velocity at $x = 0.8018$. The interface between the solid and gas at $x = 0.7415$ is sharp, and has no numerical overshoots as seen in the plots of density and ratio of specific heats. (The computed solution for the stiffening pressure is not shown, but has a behavior similar to that of the ratio of specific heats.) There are small numerical errors in the density and pressure near the trailing edge of the rarefaction at $x = 0.5010$, but these are barely visible in the plots.

Figure 4 shows enlarged views of density and pressure near the solid-gas interface and the shock in gas, respectively. These two plots illustrate the convergence behavior of the numerical solutions for increasing grid resolution. The subsequent calculations presented in this paper use the finest grid resolution shown with $h_{\text{eff}} = 1/16000$.

4.3 Shock interaction with a planar cavity: oblique incidence

As a final test, we consider the interaction of the planar shock in the solid with a gas-filled cavity when the shock is incident on the planar interface separating the solid and the gas at an acute angle β_s. When viewed in a frame of reference in which the shock and its point of intersection with the interface are stationary, the two-dimensional flow resulting from the interaction is steady provided the angle of incidence β_s exceeds a critical value. Such a steady configuration is shown in Figure 5. Interaction of the shock with the interface causes the latter to be deflected. In the gas the corresponding deflection in the flow is accommodated by the appearance of a shock, while in the solid a centered expansion fan is required to further deflect the post-shock flow such that the gas and the solid ultimately flow along the deflected interface. For the particular choice $\beta_s = 45°$ and the
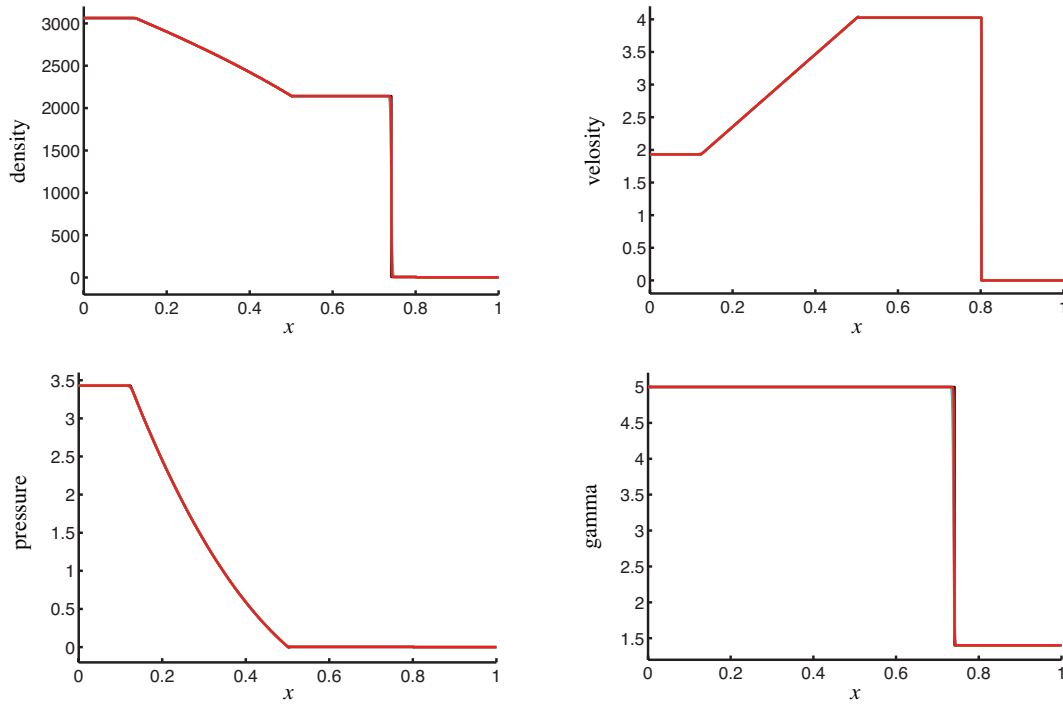
Fig. 3 Solution of the Riemann problem for the interaction of a shock in the solid with a planar solid-gas interface. Behavior of the density, velocity, pressure and ratio of specific heats (gamma) at $t = 0.06$. The exact solution is shown in black while numerical solutions with $h_{\text{eff}} = 1/4000$, $1/8000$ and $1/16000$ are shown in blue, green and red, respectively.
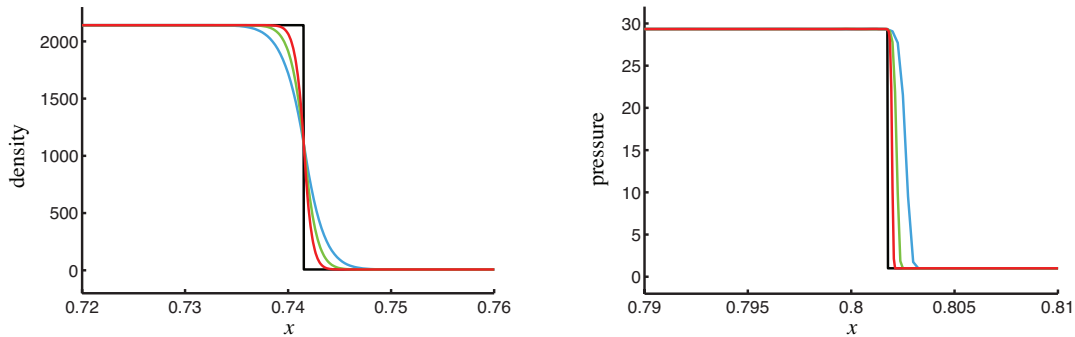

Fig. 4 Solution of the Riemann problem for the interaction of a shock in the solid with a planar solid-gas interface. Enlarged views of density and pressure at $t = 0.06$ near the interface and the shock in the gas, respectively. The exact solution is shown in black while numerical solutions with $h_{\text{eff}} = 1/4000$, $1/8000$ and $1/16000$ are shown in blue, green and red, respectively.

normal solid shock Mach number $M_{sn} = 2.0$, we compute the flow analytically and numerically and compare the corresponding results.

We let ϕ_s and ϕ_g denote a generic state variable ϕ in the solid and gas, respectively, ahead of the shocks, while $\hat{\phi}_{s2}$ and ϕ_{g2} denote the corresponding quantities downstream of the shocks. The unhatted symbol ϕ_{s2} is assigned to the state in the solid behind the expansion fan. Pressure, density and sound speed continue to be denoted by p, ρ and c, respectively. In the steady frame of reference u denotes the component normal to, and v the component tangential to, a shock,

while $q = \sqrt{u^2 + v^2}$ denotes the flow speed. The Mach angle of the flow is given by $\mu = \sin^{-1}(c/q)$ and the angle through which the flow is deflected relative to the upstream direction of the incoming flow is given by θ. Across the solid shock the normal shock conditions (4) hold, with the provision that the shock condition for the normal component of the velocity in that group is modified slightly and in an obvious way to account for the operative frame of reference in which the shock is stationary. Analogous conditions hold across the gas shock. These conditions are supplemented by the continuity constraint on the tangential component of the velocity.
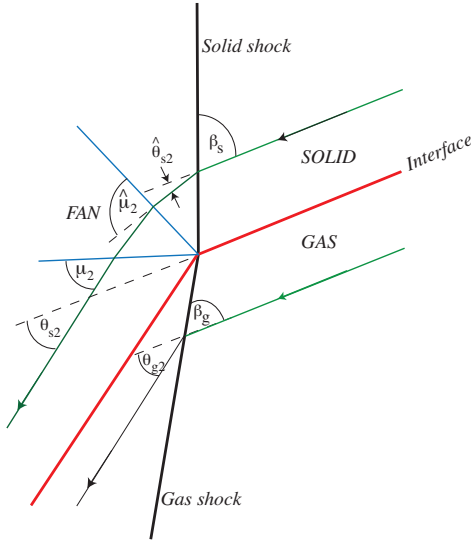
Fig. 5 Steady flow configuration for oblique shock incidence on planar interface. Flow deflection requires a shock in the gas and an expansion fan behind the shock in the solid.

Simple manipulations on the shock conditions yield the following expression for the flow deflection θ_{2g} across the gas shock,

$$\tan\theta_{2g} = \frac{2(M_{gn}^2 - 1)}{\tan\beta_g \left[(\gamma_g + 1)\frac{M_{gn}^2}{\sin^2\beta_g} - 2(M_{gn}^2 - 1)\right]},$$

where β_g is the shock inclination to the upstream flow and M_{gn} is the Mach number of the upstream flow normal to the gas shock. This relation, along with the expression for the pressure jump across the shock, constitutes a parametric description, in terms of the parameter β_g, of the p_{g2} versus θ_{g2} shock polar for the gas. Since the shock inclination angle β_s for the solid shock is presumed given, the analogous expression for the solid shock simply determines the flow deflection through the shock. The counterpart of the shock polar in the gas is the expansion-fan polar in the solid, a plot of the post-fan pressure p_{s2} against the post-fan deflection θ_{s2}. The corresponding parametric representation, in terms of the exit Mach angle μ_2 in the fan, is provided by the equation pair

$$\frac{p_{s2} + \pi_s}{\hat{p}_{s2} + \pi_s} = \left(\frac{1 + \frac{\gamma_s - 1}{2\sin^2\hat{\mu}_2}}{1 + \frac{\gamma_s - 1}{2\sin^2\mu_2}}\right)^{\frac{\gamma_s}{\gamma_s - 1}},$$

$$\theta_{s2} + P(\mu_2) = \hat{\theta}_2 + P(\hat{\mu}_2),$$

where $P(\mu)$ is the Prandtl-Meyer function

$$P(\mu) = \sqrt{\frac{\gamma_s + 1}{\gamma_s - 1}} \tan^{-1}\left(\sqrt{\frac{\gamma_s + 1}{\gamma_s - 1}} \tan\mu\right) - \mu.$$

A derivation of the above relations for an ideal gas can be found in Whitham [26] (section 6.17) and extension to a

stiffened gas is straightforward. The ultimate flow deflection and the pressure across the interface are determined by the constraint that these two quantities are continuous across the interface. The pressure-deflection plots for the solid and the gas are shown in Figure 6. The lower (supersonic) intersection of the two plots provides the acceptable solution. For the initial data supplied in Table 1, the solution yields $p_{s2} = p_{g2} = 19.77$, and $\theta_{s2} = \theta_{g2} = 17.2°$. Correspondingly, the gas shock angle and the Mach angles at the fan entrance and fan exit are, respectively, $\beta_g = 21.55°$, $\hat{\mu}_2 = 58.0°$ and $\mu_2 = 21.5°$, while the post-shock deflection angle in the solid is $\hat{\theta}_{s2} = 8.13°$ (see Figure 6). The post-fan density in the solid and the post-shock density in the gas are 2141 and 6.4, respectively.
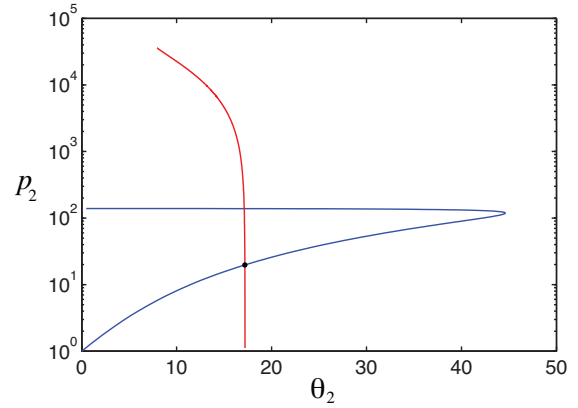

Fig. 6 Pressure versus flow deflection for the solid (expansion fan) and the gas (shock polar). The solution corresponds to the intersection of the expansion fan with the lower (supersonic) branch of the shock polar.

Figure 7 shows a comparison of the analytical and numerical solutions. The computations were carried out for a symmetric configuration in which the solid shock is incident on a gas-filled wedge of semi-angle 45°, and only the upper half of the configuration is shown. Shaded contours of density are plotted. Away from the axis of symmetry, the left view in the figure shows the steady flow in the vicinity of the point of incidence. The color bar for this frame has as its extremes the upstream density in the gas and the post-shock density in the solid. The deflected interface and the centered fan in the solid are clearly visible. A detailed comparison between the analytical and the computed solutions is made in the middle and right frames, which are enlarged views of the shaded contours of the solid and gas density in the vicinity of the point of incidence. The color bar in the solid view (middle) ranges from the analytically computed post-fan value to the post-shock value in the solid. Also shown are the analytically determined limiting rays of the fan and a line parallel to the direction of the deflected interface, all in
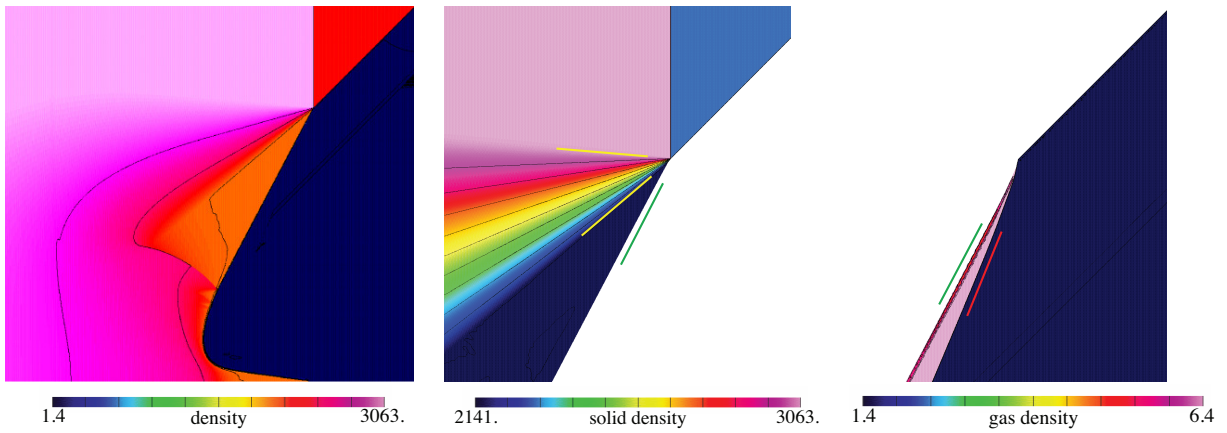
Fig. 7 Shaded contours of density (left), solid density (middle) and gas density (right) for shock interaction with an oblique planar interface. The plots of solid and gas density are enlarged views. The yellow lines show the limits of the expansion fan in the solid, the green lines provide reference angles for the interface, and the red line gives a reference angle for the shock in the gas. All lines use angles given by the exact shock-polar solution.

strong agreement with the computed solution. The density color bar in the gas view (right) ranges from the upstream value to the post-shock value in the gas. Again, the lines indicating the analytically-obtained inclinations of the interface and the gas shock are in excellent agreement with the computed solution.

5 Numerical results

This section considers in detail the principal features of the flow resulting from the interaction between a planar shock originating in the solid and an ellipsoidal gas-filled cavity embedded in the solid. The geometry of the axisymmetric configuration is shown in Figure 8. The ellipsoidal cavity is centered at the origin initially and has semi-axes a and b. The shock is located in the solid at $x = -s$ initially, and moves to the right with a velocity determined by the shock Mach number M_s. The base grid covers the numerical domain $-L \leq x \leq L$ and $0 \leq y \leq H$ with axis of symmetry $y = 0$. In the subsections below we consider four cases. The first two cases assume a spherical cavity with $a = b = 0.2$ for incident shocks with Mach numbers $M_s = 1.2$ and $M_s = 2.0$. The second two cases assume an incident shock with $M_s = 2.0$ interacting with ellipsoidal cavities with the same volume as the spherical cavity. We consider a "long cavity" (a prolate spheroid) with $a = 0.3175$ and $b = a/2$ and a "tall cavity" (an oblate spheroid) with $a = 0.1260$ and $b = 2a$. For all cases, the extent of the computational domain specified by L and H is taken to be large enough so that the behavior of the flow in the vicinity of the cavity is unaffected by the boundaries of the domain. The initial standoff distance between the shock and the leading edge of the cavity, $s - a$, is taken to be 0.1 for all cases. The calculations are performed with one refinement level and use an effective grid spacing $h_{\text{eff}} = 1/16000$. For convenience the axial direction is iden-

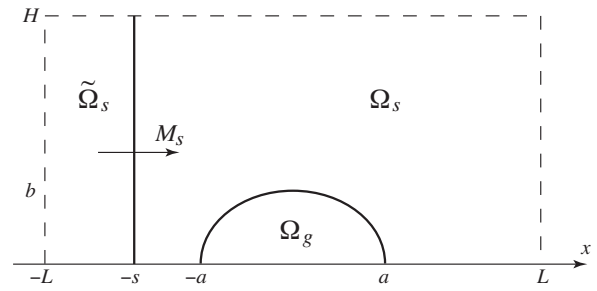tified as horizontal and the radial direction as vertical in the description below.

Fig. 8 Domain for shock-induced collapse of an ellipsoidal cavity. The ellipsoidal cavity is centered at the origin and has semi-axes a and b. The shock is located at $x = -s$ initially. The base grid covers the domain $-L \leq x \leq L$ and $0 \leq y \leq H$ with axis of symmetry $y = 0$.

5.1 Spherical cavity: $M_s = 1.2$

We begin with a discussion of the interaction of a spherical cavity and an incident shock with $M_s = 1.2$. From Table 1 we note that the dimensionless post-shock pressure in this case is $\tilde{p}_s = 5031$, and we shall be especially interested in the development of regions in the domain where this pressure is exceeded.

Following the head-on impact of the shock and the fore boundary of the cavity at $t = 0.0216$, the early stage of evolution is shown in panels (a)–(c) of Figure 9 at three selected times. At each time the corresponding horizontal panel displays shaded contours of pressure p in the solid (left), flow lines superimposed upon shaded contours of speed (middle), and shaded contours of pressure within the gas cavity (right). For ease of interpretation the cavity region is masked out in
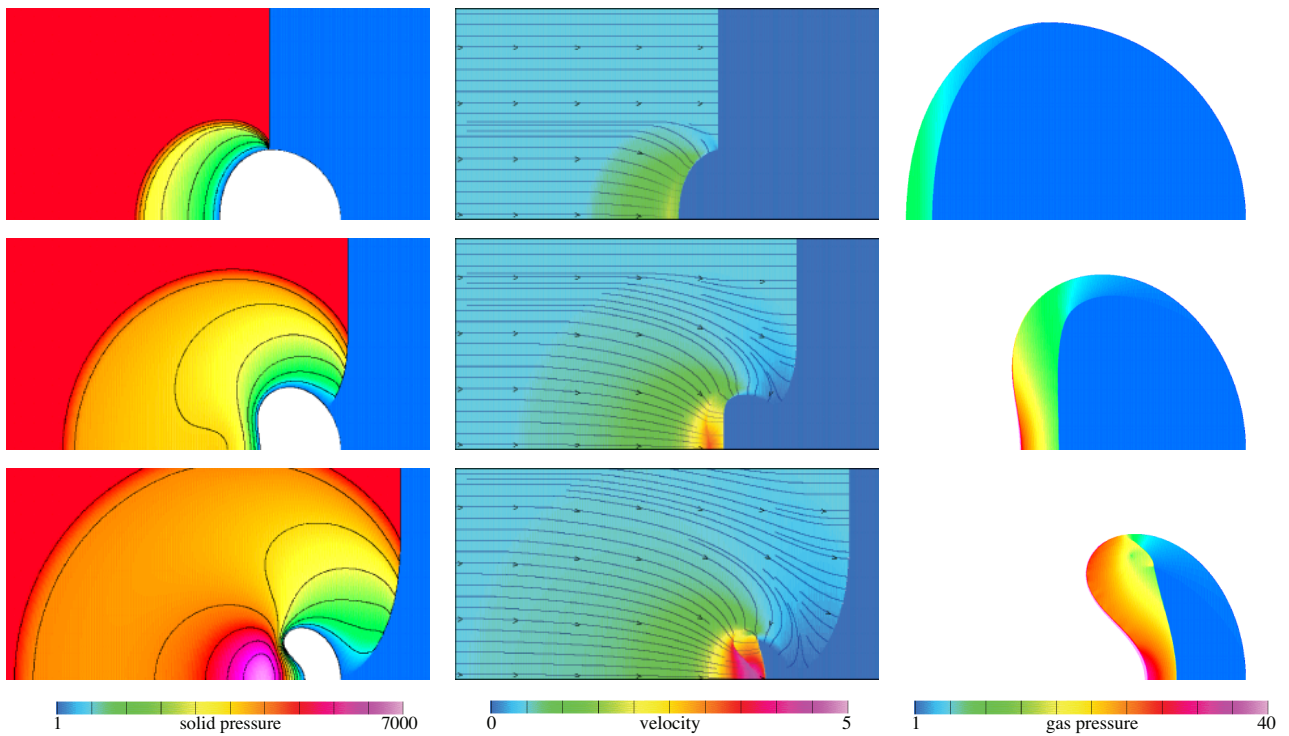
Fig. 9 Spherical cavity, $M_s = 1.2$. Shaded contours of pressure in the solid (left), magnitude of velocity (middle) and pressure in the gas (right) for shock-induced cavity collapse at times $t = 0.064$ (top row: panel (a)), $t = 0.112$ (middle row: panel (b)) and $t = 0.144$ (bottom row: panel (c)). The images of the pressure in the gas are enlarged.

white in the solid pressure plots and given a magnified view in the gas pressure plots. The range of shaded contours is given by the color bar below each image.

At $t = 0.064$, panel (a), the incident shock has reached a position nearly halfway across the cavity. The plots show that interaction with the incident shock has caused the front face of the cavity to move and deform. As the gas in the cavity has a very low acoustic impedance compared to that of the surrounding solid, a strong rarefaction is driven back into the solid while a high-Mach number shock is transmitted into the cavity. The rarefaction, best seen in the solid pressure contour plot, has led to the creation of a nautilus-shaped region of reduced pressure, narrowest at the site where the incident shock meets the interface and widest along the symmetry axis. The transmitted shock, lagging behind the incident shock due to the lower acoustic speed in the gas, is best seen in the gas pressure image, rising vertically from the symmetry axis and curving forward to meet the interface and the incident shock near the apex of the cavity. The pressure contours also show that within the region affected by the rarefaction an oblique pressure gradient is set up, causing the parallel flow entering the rarefaction front to converge towards the cavity surface. This convergence is seen clearly in the flow-line plot wherein nearly all of the flow lines that cross the rarefaction front first turn toward the interface and then experience a reverse turn as they pass through the in-

terface and enter the gas to eventually terminate normally at the transmitted shock. The result is an increase in the axial velocity and the consequent formation of a jet as the flow in the solid approaches the near-axis portion of the cavity interface. The discussion of the on-axis flow profiles later in this section will shed additional light on the formation and evolution of the jet.

At $t = 0.112$, panel (b), the incident shock has advanced further and now meets the interface at a location downstream of the apex of the cavity. The resulting diffraction of the incident shock weakens it and lends curvature to its near-interface portion, as is evident in the solid pressure and velocity plots. The fore section of the boundary of the cavity, initially spherical, has now flattened and even experienced a slight inward folding. High pressure above the cavity has caused it to shrink somewhat in the vertical direction. Meanwhile, as is evident in the plots of solid pressure and velocity, the transmitted shock has acquired the shape of an upper case gamma. The stronger portion of the transmitted shock rises vertically from the symmetry axis while the weaker portion is nearly parallel to the symmetry axis and terminates at the interface where it meets the diffracted incident shock in the solid. The flow-lines plot indicates a stronger convergence of the flow and an increased velocity along the axis of symmetry which serves to strengthen the aforementioned jet.
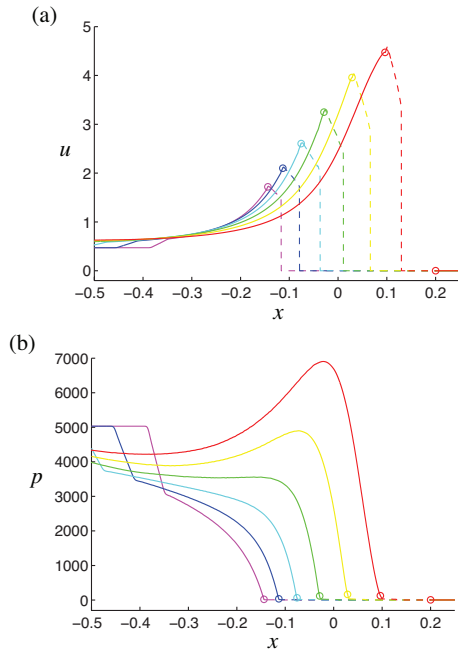
(a)

(b)

Fig. 10 Spherical cavity, $M_s = 1.2$. Profiles of (a) axial velocity u and (b) pressure p along the axis of symmetry at $t = 0.064$, 0.080, 0.096, 0.112, 0.128 and 0.144. The interface is marked by an open circle. Solid curves indicate the behavior of the solid while dashed curves show the behavior of the gas. At $t = 0.144$ the pressure peak has climbed above the pre-impact post-shock value of $\tilde{p}_s = 5031$.

At $t = 0.144$, panel (c), the upper portion of the incident shock, still planar, has moved beyond the back end of the cavity. The diffracted portion of the incident shock, now fully curved and commensurately weakened, has met the axis of symmetry at the rear of the cavity. The rarefaction front continues to propagate upstream, and has now met and passed through the numerical boundary at $y = H$. The convergence of the flow, as shown in the flow-lines plot, continues to strengthen. The result is a stronger jet which, as it pushes on the front interface, causes the latter to fold further inward into an involute. A second new feature, seen in the solid pressure plot, is the appearance of an on-axis pressure maximum upstream of the fore section of the interface. Inside the cavity the previously smooth gamma-shaped transmitted shock has now evolved into two separate branches with a kink at their junction. The main branch originating at the symmetry axis is nearly parallel to the vertical axis but with a backward lean, while the secondary branch, linked to the incident shock at the interface, is oriented at an acute angle relative to the main branch. At the kink the flow behind the shock undergoes a rapid change in direction, from nearly horizontal rightward flow behind the main branch to an inclined, mostly downward flow behind the secondary branch. From the kink has also emerged a new shock with a contact discontinuity beneath it. The faint appearance of the upper

branch of the transmitted shock in the gas pressure plot testifies to its substantially diminished strength.

Further insight into the flow thus far, and the mechanisms that have generated and modified it, can be gained by examining the on-axis behavior. Figure 10 displays the profiles of (a) axial velocity u and (b) pressure p along the symmetry axis at several times between $t = 0.064$ and 0.144. The position of the interface is marked by an open circle on each profile. The portion of the profile relevant to the solid is indicated by solid curves and that relevant to the gas by dashed curves. (The location of the interface is chosen to be the point corresponding to $w_1 = 1/(\gamma - 1) = 1.375$, midway between $w_1 = 2.5$ in the gas and $w_1 = 0.25$ in the solid.) Each velocity profile is led by the transmitted shock in the gas, across which there is a jump in velocity. The velocity continues to rise behind the shock, achieves a maximum at the interface, and then decays to its value at $x = -L$. At early times, before the rarefaction has reached the inlet, the velocity there is fixed at the post-incident-shock value. The crossing of the inlet by the rarefaction front renders the boundary into a nonreflecting surface, allowing the velocity to rise modestly to a new value that remains constant thereafter. The velocity maximum at the interface continues to rise with time, indicating the continued strengthening of the jet. However, the rate of increase begins to moderate at around $t = 0.112$, when the envelope of the velocity peaks shows a point of inflection. The strength of the transmitted shock also increases with time, as indicated by the increasing jump in velocity at the shock. The pressure scale, chosen to accommodate the maximum solid pressure, is too large to capture the pressure variations in the gas, so that the leading edge of each pressure profile essentially identifies the location of the fore boundary of the cavity. At early times the pressure profiles are monotonic and the rarefaction propagating to the left is clearly visible. At $t = 0.112$ a local maximum in the pressure is beginning to develop within the rarefaction region (as noted in the discussion above) and this maximum is seen to grow with time. We note that the magnitude of the pressure peak has risen above $\tilde{p}_s = 5031$, the pre-impact post-shock value.

The mid-time stage of evolution is shown in panels (a)–(c) of Figure 11 at three selected times. In this figure, we show shaded contours of pressure in the solid and in the gas, as before, but now have chosen to display grayscale schlieren images in the gas which highlight sharp changes in the magnitude of the gradient of density as opposed to flow line plots which do not contribute significant additional insight at this stage. Further information does accrue, however, from the histories of the on-axis profiles of u and p which are retained and displayed in Figure 12.

At $t = 0.152$, panel (a), the incident shock has gone past the aft end of the cavity and reflected off the axis. Inside the cavity the transmitted shock has advanced, along the axis,
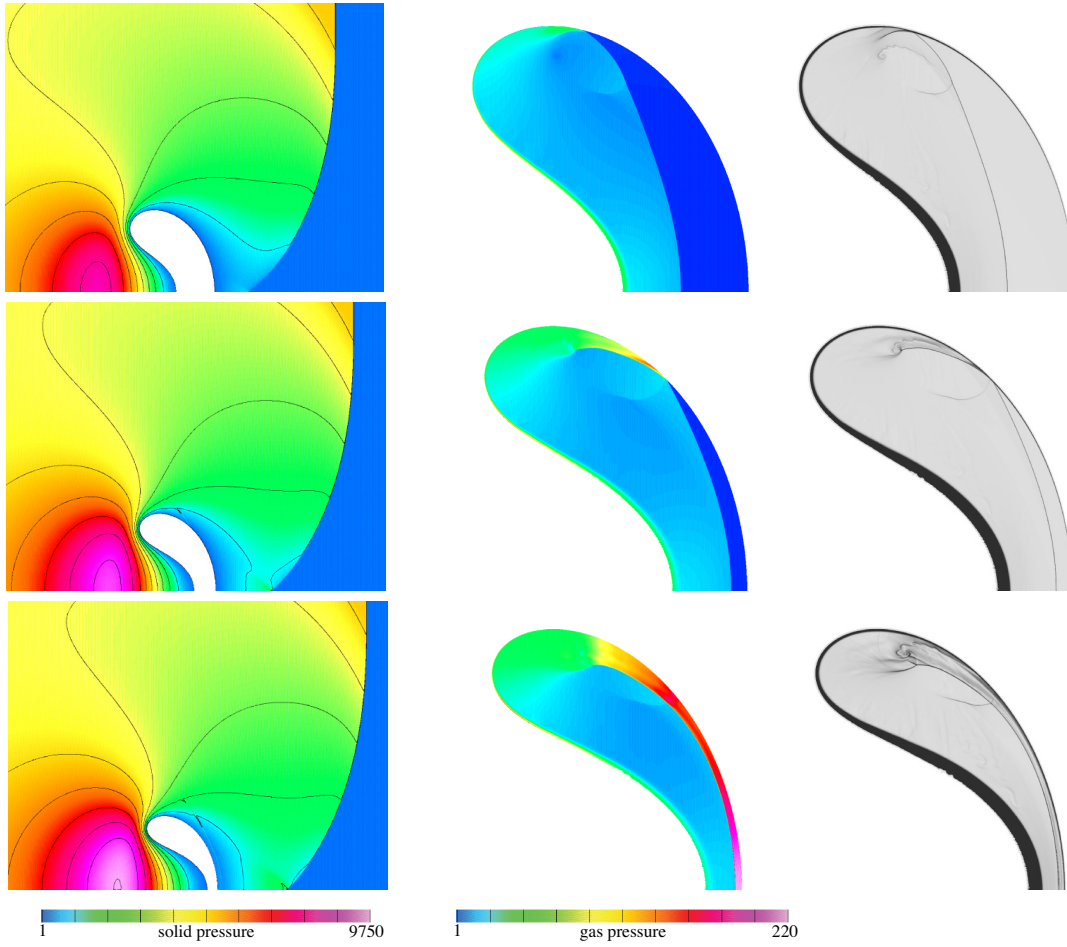
Fig. 11 Spherical cavity, $M_s = 1.2$. Shaded contours of pressure in the solid (left), pressure in the gas (middle) and numerical schlieren in the gas (right) for shock-induced cavity collapse at times $t = 0.152$ (top row: panel (a)), $t = 0.158$ (middle row: panel (b)) and $t = 0.162$ (bottom row: panel (c)). The images of pressure and numerical schlieren in the gas are enlarged.

to about the halfway mark between the involuted front and the stationary rear of the cavity, while the upper end of the transmitted shock has collided with the cavity interface at an oblique incidence. The result of the impact is a shock reflected back into the gas, as seen in the gas pressure plot and the schlieren image, and a shock transmitted into the solid, too weak to be visible in the plots at this time. The contact discontinuity first seen in the gas pressure plot at $t = 0.144$ persists and is seen to roll up, attesting to its slip-line character, while further below yet another weak shock is seen to branch off from the transmitted shock.

At $t = 0.158$, panel (b), the transmitted shock in the gas has nearly reached the rear of the cavity along the axis. The site of oblique impact of the upper end of this shock with the cavity interface, and the associated gas-dynamic structure within the cavity, have moved closer to the axis. The shock transmitted into the solid as a result of the impact is now visible in the shaded contour plot of solid pressure as a small blip in the contour lines, while the shock reflected back into

the gas has now interacted with, and moved beyond, the slip line.

At $t = 0.162$, panel (c), the transmitted shock, subsequent to a collision with the rear wall of the cavity at a time instant between $t = 0.158$ and $t = 0.162$, has reflected back and is now moving from right to left within the cavity. This collision was nearly normal due to the transmitted shock and the aft section of the interface having similar curvature. As a result, we see a ribbon of high pressure in the gas behind the shock near the rear of the cavity. The shock transmitted into the solid as a result of the collision, although still weak, can be seen as a small disturbance in the shaded contour plot of solid pressure.

As before, we find it helpful to consider the on-axis profiles of u and p. These are displayed in Figure 12 for $t = 0.152$ to $t = 0.162$ in time intervals of 0.002. The large-scale profiles of u (Figure 12(a)) show a mild temporal increase in the velocity of the jet and a correspondingly mild increase in the strength of the transmitted shock in the gas. The large-scale profiles of p (Figure 12(b)) show that the
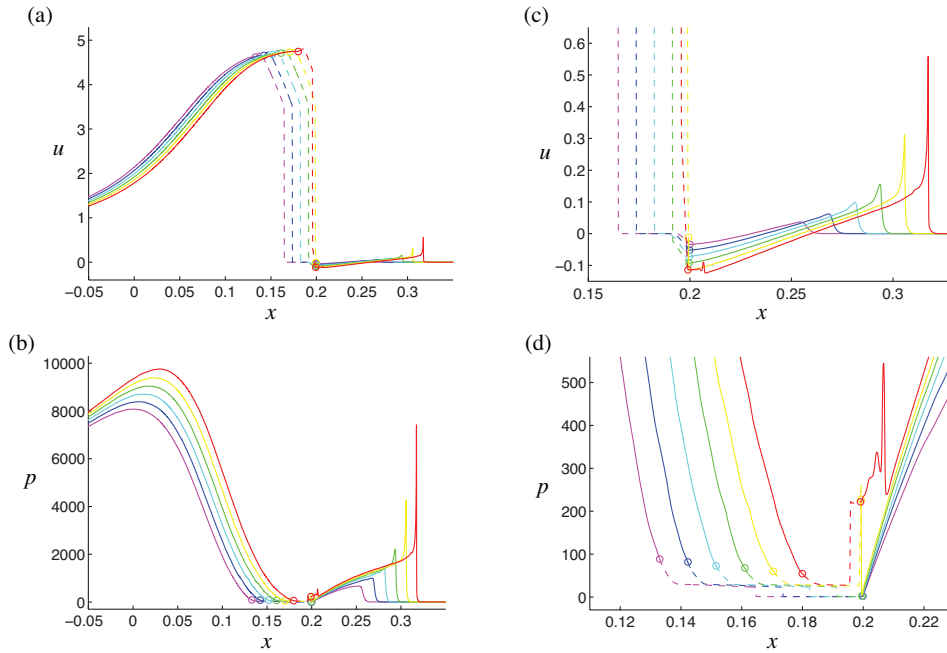
Fig. 12 Spherical cavity, $M_s = 1.2$. Profiles of (a,c) axial velocity u and (b,d) pressure p along the axis of symmetry at $t = 0.152, 0.154, 0.156, 0.158, 0.160$ and 0.162. The interface is marked by an open circle. Solid curves indicate the behavior of the solid while dashed curves show the behavior of the gas. At $t = 0.162$ the pressure peak in the solid is nearly twice the pre-impact post-shock value of 5031.

lead disturbance along the axis, generated by the collision of the incident shock in the solid with the axis, is a shock whose strength increases with time, and has grown above the initial post-shock pressure of $\tilde{p}_s = 5031$. The cause of this increase is the progressively higher strength of the incident shock itself; the further away from the aft end of the cavity the lead shock is when it collides with the axis, the weaker is the diffraction it has suffered in going around the cavity. The pressure profiles also show a steady increase in the pressure maximum upstream of the cavity, to levels more than twice as high as the post-shock pressure prior to impact.

Additional details can be gleaned from Figures 12(c) and (d) which show enlarged views of the profiles near the aft end of the cavity. In the enlarged velocity profiles, we note that behind the lead shock in the solid the velocity drops, even to negative values, reaches a minimum at the interface, and then rises on the gas side before undergoing a jump at the transmitted shock in the gas. The zoomed profiles of pressure show the advance of the transmitted shock in the gas towards the aft end of the cavity. As noted earlier, the transmitted shock has almost reached the cavity at $t = 0.158$. At $t = 0.160$, the transmitted shock is flush with the interface itself, and at $t = 0.162$ it has reflected off the interface and is propagating back into the gas with a significantly increased value of pressure behind it. The resulting behavior in the solid, at $t = 0.162$, shows a sharp rise in pressure behind the transmitted shock which is traveling forward

away from the cavity and into the region already processed by the incident shock.

The late-time stage of evolution begins with the rightward traveling high-speed jet first impacting the leftward-traveling shock in the gas, and then the rear interface of the cavity. This catastrophic event, occurring between $t = 0.162$ and $t = 0.165$, collapses the near-axis portion of the cavity, squeezing out nearly all of the gas contained therein and splitting the cavity into an annular ring. It is convenient to follow the post-collision events by continuing our examination of the on-axis behavior, as displayed in the on-axis profiles of u and p in Figure 13 for times $t = 0.165, 0.166$ and 0.167. Since numerical diffusion has broadened the leading edge of the jet, the immediate result of the impact is the creation of a finite-width pressure pulse that takes a finite, albeit short, time to build from a pre-collapse level of $p \approx 200$ (see Figure 12(d)) to the enormously high post-collapse level of $p \approx 45,000$ at $t = 0.167$ (Figure 13(b)). This value represents a nearly nine-fold increase as compared to the initial post-shock value of $\tilde{p}_s = 5031$. As the pulse builds it also steepens at either end, leading to the emergence of two shocks. The rightward-traveling shock faces a solid region that has been processed by the incident shock and has thereby acquired a weak backward flow, while the leftward-traveling shock advances against the high-speed jet (Figure 13(a)). The region between the shocks is noisy, and we shall discuss the origin of the noise below when we consider shaded contour plots of the flow. The on-axis development
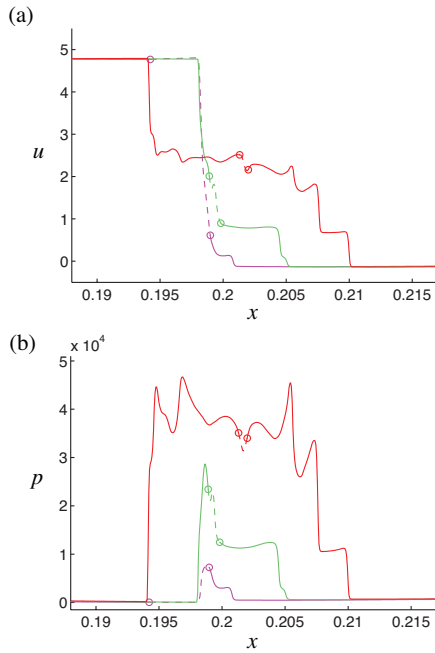
Fig. 13 Spherical cavity, $M_s = 1.2$. Profiles of (a) axial velocity u and (b) pressure p along the axis of symmetry at $t = 0.165$, 0.166 and 0.167. The interface is marked by an open circle. Solid curves indicate the behavior of the solid while dashed curves show the behavior of the gas.

Fig. 14 Spherical cavity, $M_s = 1.2$. Profiles of (a) axial velocity u and (b) pressure p along the axis of symmetry at $t = 0.168$, 0.176 and 0.184.

at later times is shown in the profiles of u and p at $t = 0.168$, 0.176 and 0.184 in Figure 14. Both sets of profiles show a gradual diminution in the strength of either shock with the passage of time. Nevertheless, even at times as late as $t = 0.184$ the pressure within the blast region between the two shocks retains elevated levels more than four times the initial post-shock pressure. We also note in Figure 14 that a small amount of gas remains trapped in the post-collapsed flow. This is a remnant of the collapsed interface of the cavity, which we discuss in more detail below.

With the on-axis behavior well in hand, a further understanding of the global events accompanying the collapse of the gas cavity is achieved by examining Figure 15, which displays in panels (a)–(d) the evolutionary sequence over the same range of time as was used in Figure 14. With the gas cavity masked in white, a long view of pressure evolution in the solid is shown in the shaded contour plots of pressure in the left column. Pressure evolution inside the cavity and within a close vicinity of the cavity is shown in the expanded views of the middle column. These images have greyscale schlierens superimposed to better highlight shocks and contacts. The right column displays shaded contours of w_1, again in an expanded view.

The images at $t = 0.168$ are shown in panel (a). The left image shows the early development of the post-collapse blast, the region of high pressure bounded by shocks traveling outwards. The shock traveling leftwards is stronger, and
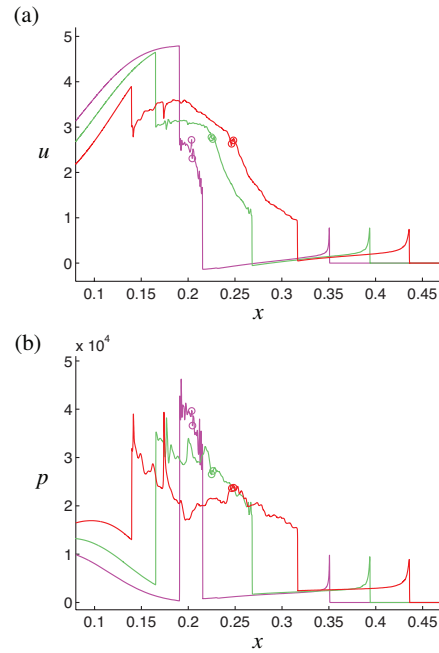
as remarked above, advances more slowly than the one on the right. The middle image focuses on the events within the cavity where the principal features include the reflected shock traveling leftwards and now situated nearly in the middle of the cavity, and a narrow region of high pressure at the lower end of the cavity, created by the criss-crossing of reflected shocks within the wedge bounded by the two cavity interfaces. The shaded contour of w_1 in the right image shows the outline of the cavity and the thin ribbon (more precisely, a cross-section of the thin surface) that connects it to the axis and is a remnant of the collapsed interface.

The images at $t = 0.176$ are shown in panel (b). The solid-pressure plot on the left shows an expansion of the blast region between the two shocks and a shrinkage in the size of the cavity. The high-speed jet continues to impede the advancement of the leftward-traveling shock while the rightward-traveling shock, relatively unhindered, increasingly approximates a spherical blast wave. Both shocks lose strength as they advance, the rightward-traveling shock more so than its leftward-traveling twin, and the highest pressures continue to be found on the axis. Also visible in this image is a band of compressive disturbances emanating into the solid from the wedge-shaped rear of the cavity, about which more will be said below. The pressure plot in the middle and the plot of w_1 on the right provide further details of the features within and around the cavity. The middle image shows that the region of elevated pressure that originated at the apex of the wedge has now expanded to occupy about a third of the
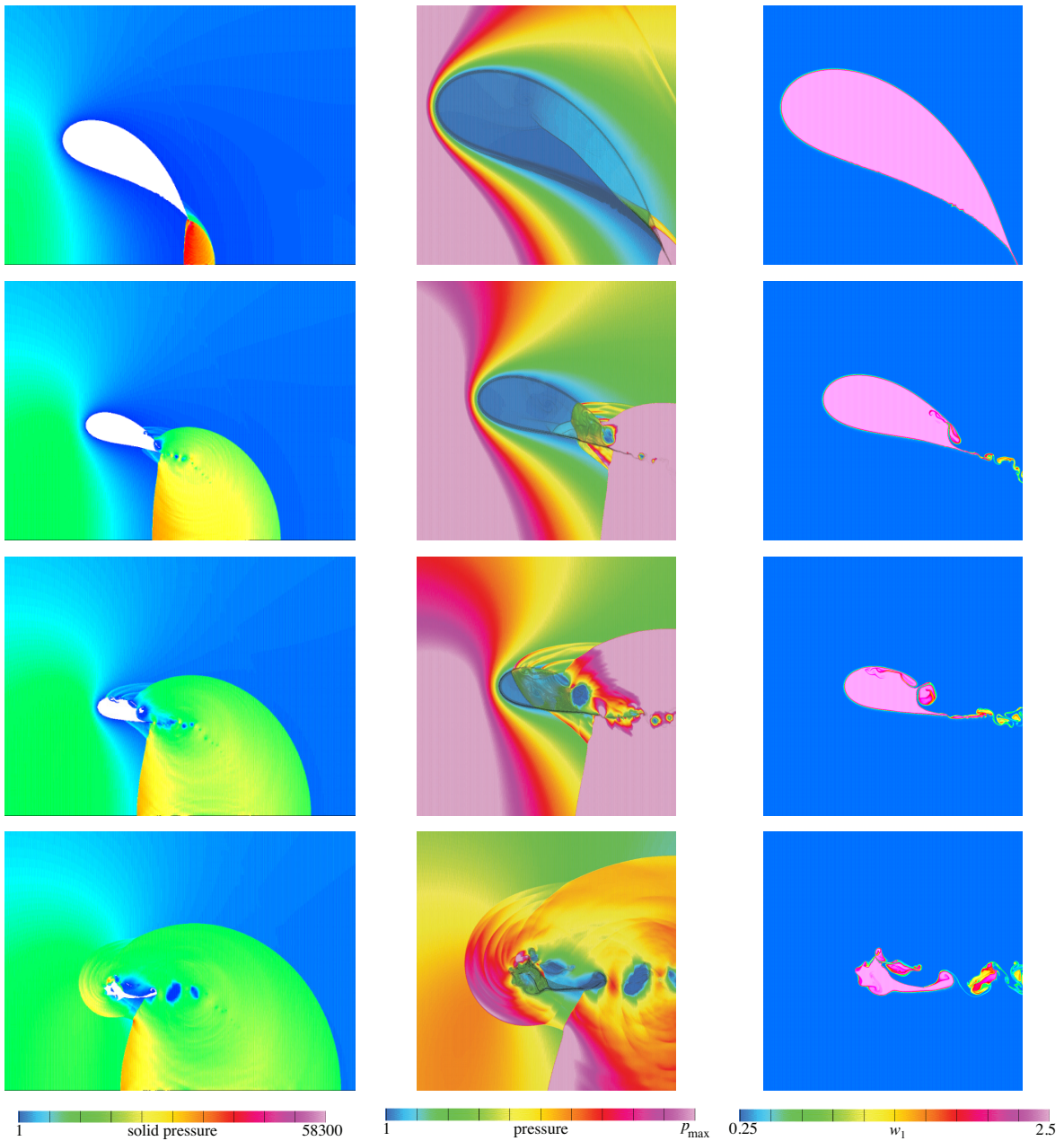
Fig. 15 Spherical cavity, $M_s = 1.2$. Shaded contours of pressure in the solid (left), enlarged views of pressure in the solid and gas (middle), and w_1 (right) for shock-induced cavity collapse at times $t = 0.168$ (top row: panel (a)), $t = 0.176$ (second row: panel (b)), $t = 0.180$ (third row: panel (c)) and $t = 0.184$ (bottom row: panel (d)). Color bars indicate the range of contours with $p_{max} = 4000$, 8000, 12000 and 28000 for panels (a), (b), (c) and (d), respectively. The middle-column views show regions of pink color in the high-pressure region ahead of the cavity and in the blast region below the cavity. In these two regions, the pressure is higher than the maximum value for the color range chosen for the plot and thus the color table is saturated there.

cavity. At the same time, the right image reveals that a channel has developed at the tip of the wedge through which solid at high-pressure has intruded into the cavity in the form of a slender jet. The jet hugs the upper wall of the cavity and undergoes multiple reflections against this wall. Thus the band of compressive waves that extend into the solid from the cavity are a result both of the elevated pressure within the cavity generated by the network of criss-crossing shock waves, and the impingement of the jet against the upper wall of the cavity. As a result these waves, especially those transmitted into the solid from the upper wall of the cavity, exhibit a sequence of discrete pressure peaks clearly revealed in the middle image. We also observe, in the right image, that the thin vortex sheet connecting the cavity to the axis, entraining a small amount of gas that has been squeezed to high pressures, has begun to roll up. While the sheet is physical in
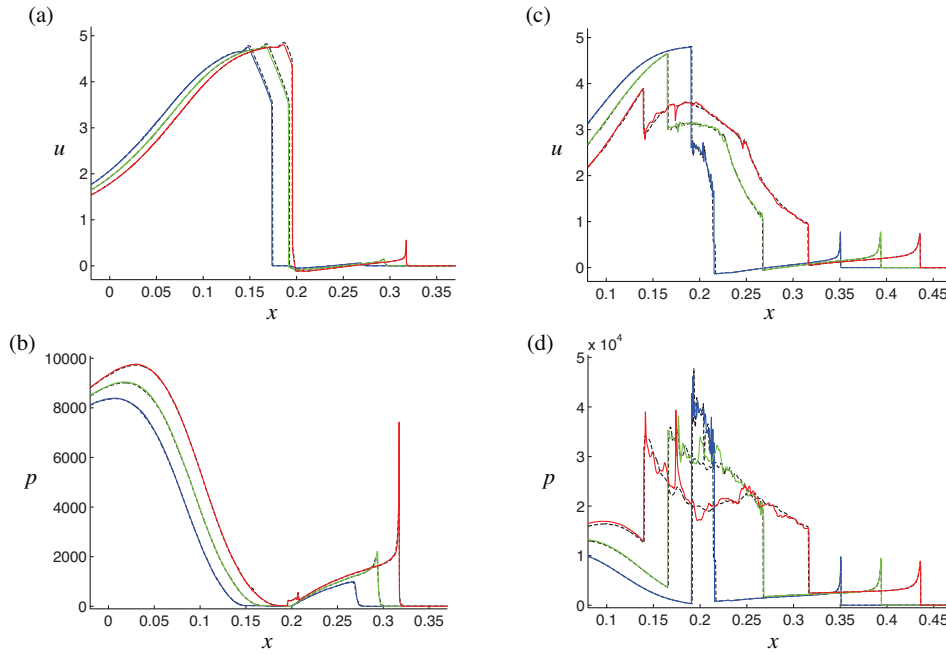
Fig. 16 Spherical cavity, $M_s = 1.2$. Profiles of (a) axial velocity u and (b) pressure p along the axis of symmetry at $t = 0.154, 0.158$ and 0.162, and (c) u and (d) p at $t = 0.168, 0.176$ and 0.184. Solid curves show the behavior of the solid and gas for a fine-grid calculation with $h_{\text{eff}} = 1/16000$ while dashed curves show the behavior of the solid and gas for a coarse-grid calculation with $h_{\text{eff}} = 1/8000$.

origin, its exact makeup is a numerical construct, based on the amount of artificial diffusion inherent to the numerical method. As gas-dynamic disturbances in the high-pressure region within which the sheet is located interact with the sheet, a certain amount of noise is generated that is manifest both in the on-axis plots of Figures 13 and 14 and the shaded pressure contours in the left column of Figure 15.

The images at $t = 0.180$ are shown in panel (c). The blast region continues its expansion and the cavity its shrinkage, as shown in the left image. The rightward-traveling shock bounding the blast surrounds an increasing portion of the cavity across the upper cavity wall. Within the cavity, the middle and right images show that the thin jet of solid continues to advance along the upper wall, suffering additional collisions and transmitting the resulting pressure pulses into the solid. The region of elevated pressure within the cavity, now led by a single shock front, has moved closer to the front of the cavity.

The images at $t = 0.184$ are shown in panel (d). The left image shows that the cavity is now almost completely encased within, and further squeezed by, the high-pressure blast region. Within the cavity the leftward-traveling shock front and the infiltrating solid jet have both collided with the front face of the cavity, thereby propelling yet new and stronger pressure disturbances into the solid. As the middle image shows, the pressure at the head of these disturbances is of comparable magnitude to the pressure behind the leftward-traveling shock bounding the blast region, and

the collision of these two fronts, in due course, will generate even larger local pressures in the solid.

In view of the complex dynamics occurring in the process of cavity collapse, it is worth making a further assessment of the accuracy of the numerical results, especially at later times in the evolution. Figure 16 shows the on-axis behavior of u and p at three times just prior to the impact of the jet with the aft side of the cavity (plots (a) and (b)) and at three times just after the collapse (plots (c) and (d)). The solid curves in the figure show the results from the fine-grid calculation with $h_{\text{eff}} = 1/16000$ while the dashed curves show the corresponding results from a coarser-grid calculation with $h_{\text{eff}} = 1/8000$. The excellent agreement indicates that the shocks and the interface prior to collapse, and the oppositely-traveling blast waves subsequent to collapse, are accurately computed on the fine grid. Small discrepancies between the coarse and the fine-grid results do appear, but these are confined to the details of the noise generated in the region between the blast waves, as seen in the plot of p in Figure 16(d). Figure 17 shows shaded contours of the solid pressure and enlarged views of pressure and w_1 in the vicinity of the gas cavity at $t = 0.080$ in the post-collapsed state. Fine-grid results are shown in the top row (panel (a)) while coarse-grid results are shown in the bottom row (panel (b)). Excellent agreement is observed in the overall view of the solid pressure, indicating again that the position of the now collapsed interface and the strength and location of the blast waves in the solid are computed accurately. The enlarged
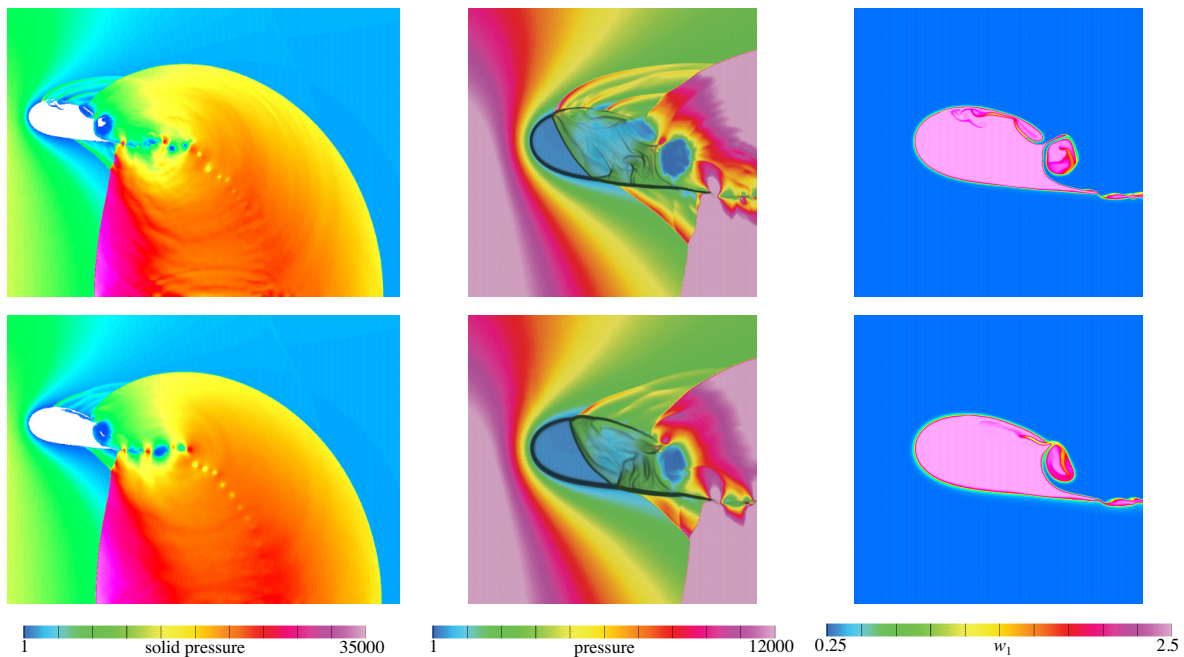
Fig. 17 Spherical cavity, $M_s = 1.2$. Shaded contours of pressure in the solid (left), enlarged views of pressure in the solid and gas (middle), and w_1 (right) for shock-induced cavity collapse at time $t = 0.180$. The top row (panel (a)) shows the behavior for a fine-grid calculation with $h_{eff} = 1/16000$ while bottom row (panel (b)) shows the behavior for a coarse-grid calculation with $h_{eff} = 1/8000$. The middle-column views show regions of pink color in the high-pressure region ahead of the cavity and in the blast region below the cavity. In these two regions, the pressure is higher than the maximum value for the color range chosen for the plot and thus the color table is saturated there.

views of pressure and w_1 also show good agreement as to the broad features of the flow within and around the cavity, but some differences do appear in the fine-scale details resulting from the collapse of the cavity and the interaction of the aforementioned thin jet of solid with the interface. In particular, the progress of the thin jet is slightly delayed in the coarse-grid results, thereby affecting the forward movement of the principal shock within the cavity and the pattern of the pressure bursts emanating from the cavity into the solid. The evolution of this thin jet is particularly difficult to compute with high accuracy and would require very high grid resolution.

5.2 Spherical cavity: $M_s = 2.0$

We now turn to the case $M_s = 2.0$ corresponding to the larger of the two Mach numbers considered. The following description will emphasize only those features that are in contrast with the lower Mach number case considered above; where the response is similar we shall be content with a brief description or simply a reference to the earlier case. From Table 1 we note that the dimensionless post-shock pressure is $\tilde{p}_s = 34300$, a considerably larger value than that of the previous $M_s = 1.2$ case.

The first stage of evolution, characterized by the events that take place immediately prior to the on-axis collision of

the transmitted shock within the cavity with the back wall of the cavity, is summarized in Figures 18 and 19. Figure 18 displays information at three selected times, in the same format as that employed earlier for $M_s = 1.2$ in Figure 9. The corresponding series of events for $M_s = 1.2$ was captured in Figures 9–12, over a time span identified there as comprising two stages of evolution, the early stage and the mid stage. Here the development is faster in several respects due to the higher Mach number of the incident shock, and many features of the earlier case are retained. Thus we observe once again the appearance of the rarefaction in the solid and the transmitted shock in the gas, the convergence of the flow lines in the solid to form a jet, the growing on-axis pressure bump in the solid, and the inward folding of the front face of the cavity.

Other features of the development are different than the $M_s = 1.2$ case. Foremost among these is the chain of processes within the cavity, now showing a somewhat greater complexity and further revealed in the schlieren images shown in Figure 19. These images present magnified views within the cavity and are displayed at three instants of time, comprising approximately the same time interval as that in Figure 18. The transmitted shock, which started out with a smooth, gamma-shaped profile at earlier times (see Figure 18) has developed a kink at $t = 0.052$. This kink, and the secondary discontinuities (a shock and a slip line) emerging therefrom, mimic similar behavior seen for $M_s = 1.2$; see Figure 9,
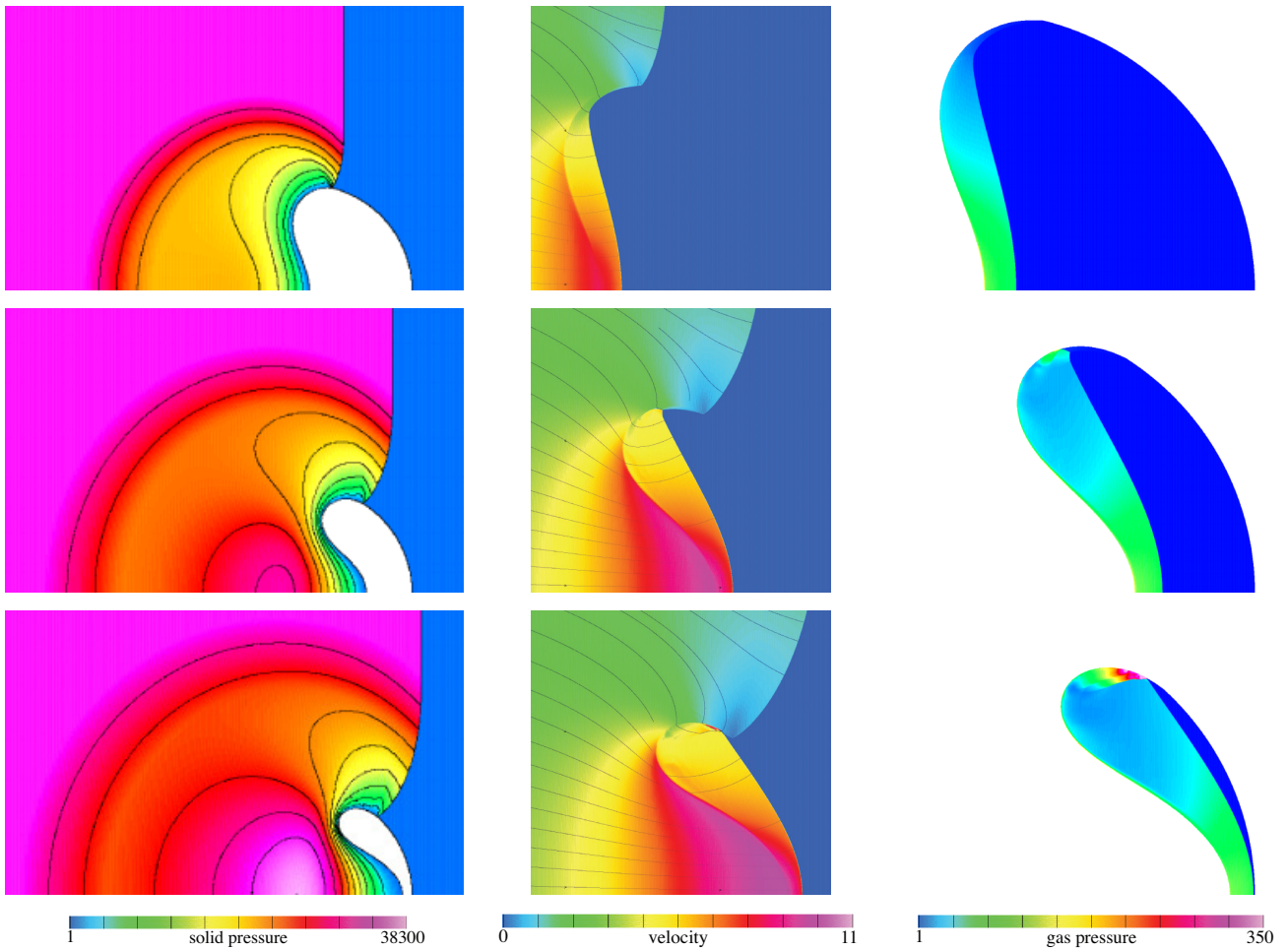
Fig. 18 Spherical cavity, $M_s = 2.0$. Shaded contours of pressure in the solid (left), magnitude of velocity (middle) and pressure in the gas (right) for shock-induced cavity collapse at times $t = 0.048$ (top row: panel (a)), $t = 0.060$ (middle row: panel (b)) and $t = 0.067$ (bottom row: panel (c)). The images of the magnitude of velocity and pressure in the gas are enlarged.

Fig. 19 Spherical cavity, $M_s = 2.0$. Numerical schlieren images in the cavity at times $t = 0.052$ (left), $t = 0.060$ (middle) and $t = 0.067$ (right).

panel (c). However, at $t = 0.060$ a second kink with its own pair of discontinuities emerges, even as the pattern attached to the first kink undergoes a reflection at the cavity wall (middle image). The various discontinuities interact mutually, as well as with the cavity wall, yielding an overall structure that contains rolled-up slip lines and multiply reflected shocks (right image). A second difference is in the progress

of the incident shock which, in the $M_s = 1.2$ case, had gone completely around the cavity by the end of the early stage of evolution (Figure 9, panel (c)), and met the axis of symmetry. By the time the transmitted shock in the gas had made its way to the rear wall of the cavity, the incident shock had progressed substantially beyond the trailing end of the cavity and reflected off the axis (Figure 11, panel (b)). Here, while
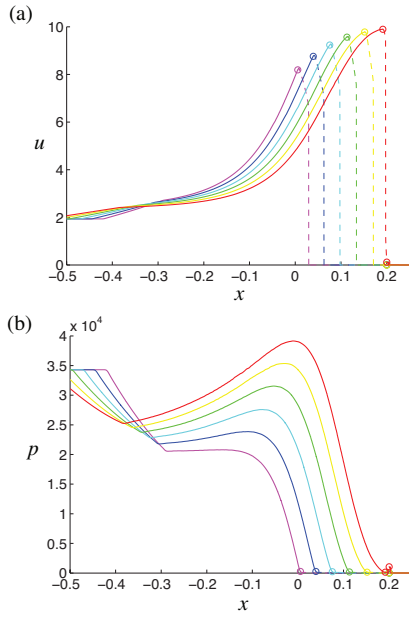
(a)

(b)

Fig. 20 Spherical cavity, $M_s = 2.0$. Profiles of (a) axial velocity u and (b) pressure p along the axis of symmetry at $t = 0.048, 0.052, 0.056, 0.060, 0.064$ and 0.068. The interface is marked by an open circle. Solid curves indicate the behavior of the solid while dashed curves show the behavior of the gas. The pressure peak in the solid has risen modestly above the initial post-shock value of $\tilde{p}_s = 34300$.

(a)

(b)

Fig. 22 Spherical cavity, $M_s = 2.0$. Profiles of (a) axial velocity u and (b) pressure p along the axis of symmetry at $t = 0.072, 0.076, 0.080$ and 0.084.

the transmitted shock has nearly completed its forward passage through the cavity, the incident shock, along the interface, has hardly gone beyond the apex of the cavity (Figure 18, panel (c)). A third difference is seen in the sequence of on-axis profiles of u and p in Figure 20. Even though there is a qualitatively similarity with Figures 10 and 12, with the u profiles showing the initially rapid but then more subdued acceleration of the jet and the p profiles displaying the continued growth of the pressure bulge within the rarefaction, there are substantial quantitative differences. The jet velocity is now more than twice as high, and the pressure maximum four times larger, than was the case for $M_s = 1.2$ (see Figure 12). We note, however, that in relative terms the pressure peak is only modestly above the initial pre-shock value of 34300.

We now consider the second phase of evolution, which begins with the collision of the jet-driven front face of the cavity with the rear face, and continues through the process of cavity collapse. It is displayed in panels (a)–(c) of Figure 21 at three selected times. This figure employs the same format as Figure 15 for $M_s = 1.2$. As before, the middle-column views show regions of pink color in the high-pressure region ahead of the cavity and in the blast region below the cavity. In these two regions, the pressure is higher than the maximum value for the color range chosen for the plot and thus the color table is saturated there. The principal feature of cavity collapse will again be the splitting of the cavity
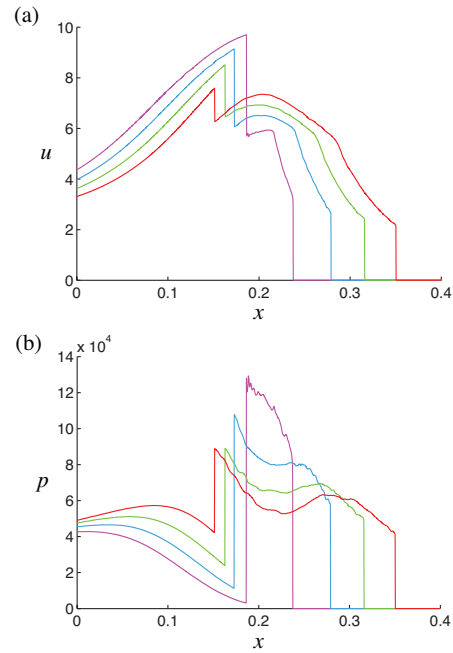
followed by the creation of an expanding region of high pressure within the solid, bounded by outwardly propagating blast waves. As for $M_s = 1.2$, we shall again see the penetration of the cavity by a slender high-speed jet of solid, and the microblasts released into the solid by the repeated impingement of the jet against the cavity wall. A new feature will be the interaction of the rightward propagating blast with the incident shock. We now describe the evolution in some detail.

At $t = 0.072$, panel (a), the transmitted shock, last seen in Figure 18, panel (c), and approaching the rear of the cavity, has now reflected off the rear wall of the cavity in its entirety. The primary feature within the cavity, best seen in the middle pressure plot, is again a tribrachial shock. The collision of the transmitted shock with the cavity has also sent a weak shock into the solid. The jet has impacted the rear interface and split the cavity into a toroidal shape in a similar way as for $M_s = 1.2$. The impact, as before for the lower Mach number, has led to the creation of a high-pressure solid region, with blast waves advancing both leftwards and rightwards (upper left image). In the lower, wedge-shaped end of the cavity, internal shock reflections have again created a local cell of high pressure. As these shocks advance up the wedge, they leave in their wake an expanding slug of high pressure that extends into the solid. Once again at the apex of the wedge there appears a slender jet of high-pressure solid penetrating the cavity. This jet can be seen in the plots of w_1 at later times (right images, panels (b) and (c)).
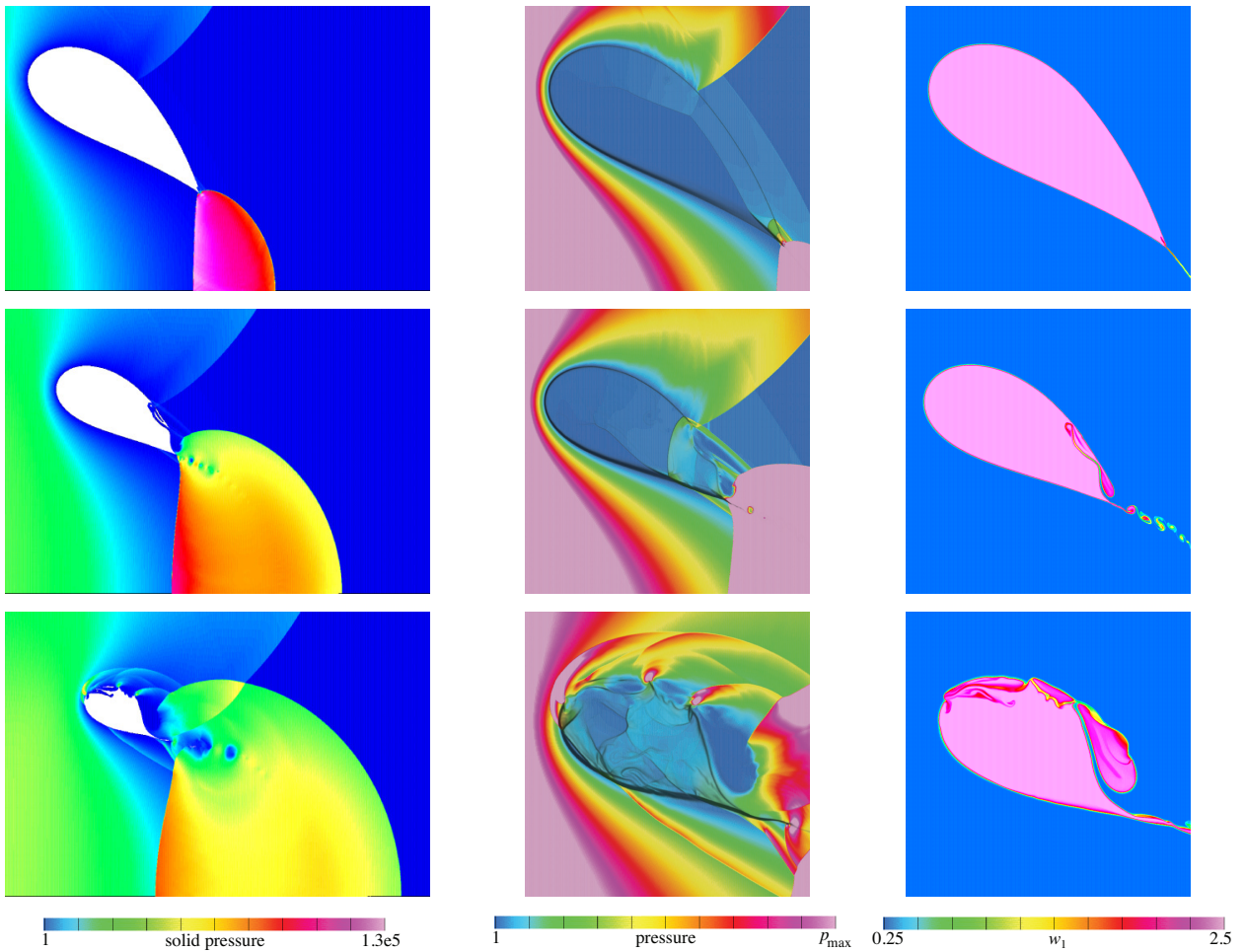
Fig. 21 Spherical cavity, $M_s = 2.0$. Shaded contours of pressure in the solid (left), enlarged views of pressure in the solid and gas (middle), and w_1 (right) for shock-induced cavity collapse at times $t = 0.072$ (top row: panel (a)), $t = 0.076$ (middle row: panel (b)) and $t = 0.080$ (bottom row: panel (c)). Color bars indicate the range of contours with $p_{max} = 15000$, 20000 and 30000 for panels (a), (b) and (c), respectively. The middle-column views show regions of pink color in the high-pressure region ahead of the cavity and in the blast region below the cavity. In these two regions, the pressure is higher than the maximum value for the color range chosen for the plot and thus the color table is saturated there.

At $t = 0.076$, panel (b), the incident shock has begun to interact with the high-pressure slug (middle pressure image). As for $M_s = 1.2$, the slender jet undergoes repeated collisions with the upper interface of the cavity, thereby sending a discrete sequence of strong pressure waves into the solid.

At $t = 0.080$, panel (c), the slender jet has begun to go around the nose of the cavity. By this time the cavity has shrunk to a fraction of its original size, and the interaction between the incident shock and the cavity has led to the establishment of a complex structure consisting of a number of high-pressure regions. These include the broadening but decaying blast set up by the main jet, a discrete sequence of micro-blasts caused by the slender jet infiltrating through the cavity, and a wider region behind the cavity where the main blast and the incident shock interact. The highest pressure is still found on the axis behind the leftward traveling shock

forming the edge of the blast. The on-axis plots in Figure 22 illustrate the growth and decay of the blast. We note that in contrast to Figure 14 for $M_s = 1.2$, the maximum pressure in the solid region and the maximum jet velocity are now nearly twice as large. In relative terms, however, the immediately post-collapse pressure maximum of 130000, at $t = 0.072$, is nearly four times the pre-impact post-shock value of 34300. Also, at the last time shown, $t = 0.084$, the pressure within the blast region between the two shocks remains at levels above the initial post-shock pressure.

5.3 Long cavity (prolate spheroid): $M_s = 2.0$

In this section we examine the response of an ellipsoidal cavity in the shape of a prolate spheroid, with the major axis twice as long as the minor axis and volume equal to the that of the spherical cavity considered in the preceding
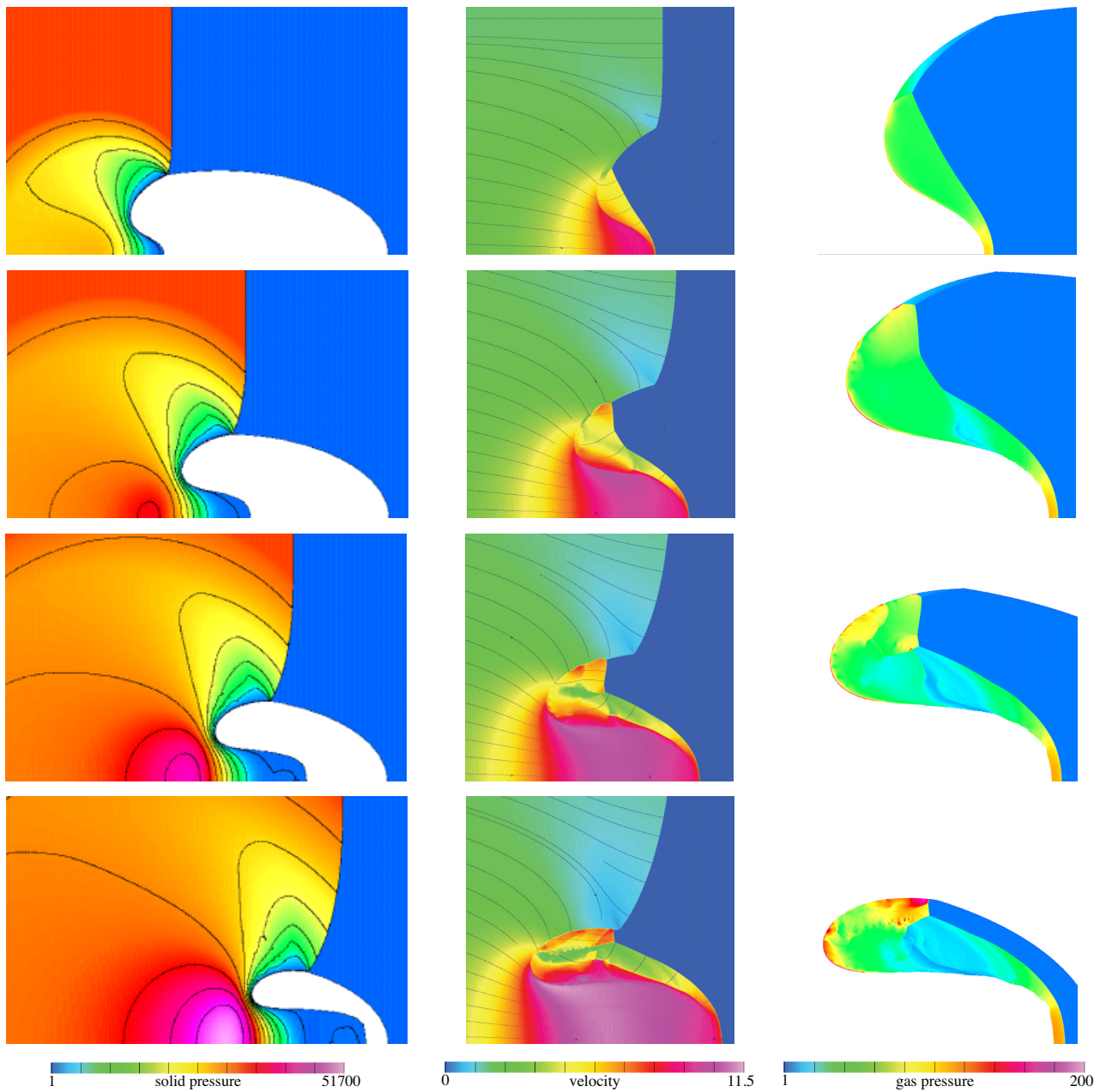
Fig. 23 Long cavity, $M_s = 2.0$. Shaded contours of pressure in the solid (left), magnitude of velocity (middle) and pressure in the gas (right) for shock-induced cavity collapse at times $t = 0.042$ (top row: panel (a)), $t = 0.060$ (second row: panel (b)), $t = 0.072$ (third row: panel (c)) and $t = 0.084$ (bottom row: panel (d)). The images of the magnitude of velocity and pressure in the gas are enlarged.

sections. The intent is to determine the extent to which the shock-induced response, in qualitative as well as quantitative aspects, is affected by the shape of the cavity. The Mach number of the incident shock is taken to be $M_s = 2.0$ corresponding to the stronger of the two values considered previously for the spherical cavity.

The early stage of evolution shown in Figure 23 is visualized in the same format as Figure 18. The images are chosen at four selected instants of time. At $t = 0.042$, panel (a), the impact has led to the by-now familiar appearance of a rarefaction in the solid and a transmitted shock in the cavity. Also, the front face of the cavity has already undergone an involution, streamline convergence and jet formation have taken place, and a pressure maximum has appeared on the axis. The gamma-shaped transmitted shock has acquired the kinked profile and associated gasdynamic discontinuities seen earlier in the spherical configuration. A slight curvature near the impact point with the cavity shows the weakening of the incident shock. At $t = 0.060$, panel (b), the incident shock has gone past the apex of the long cav-
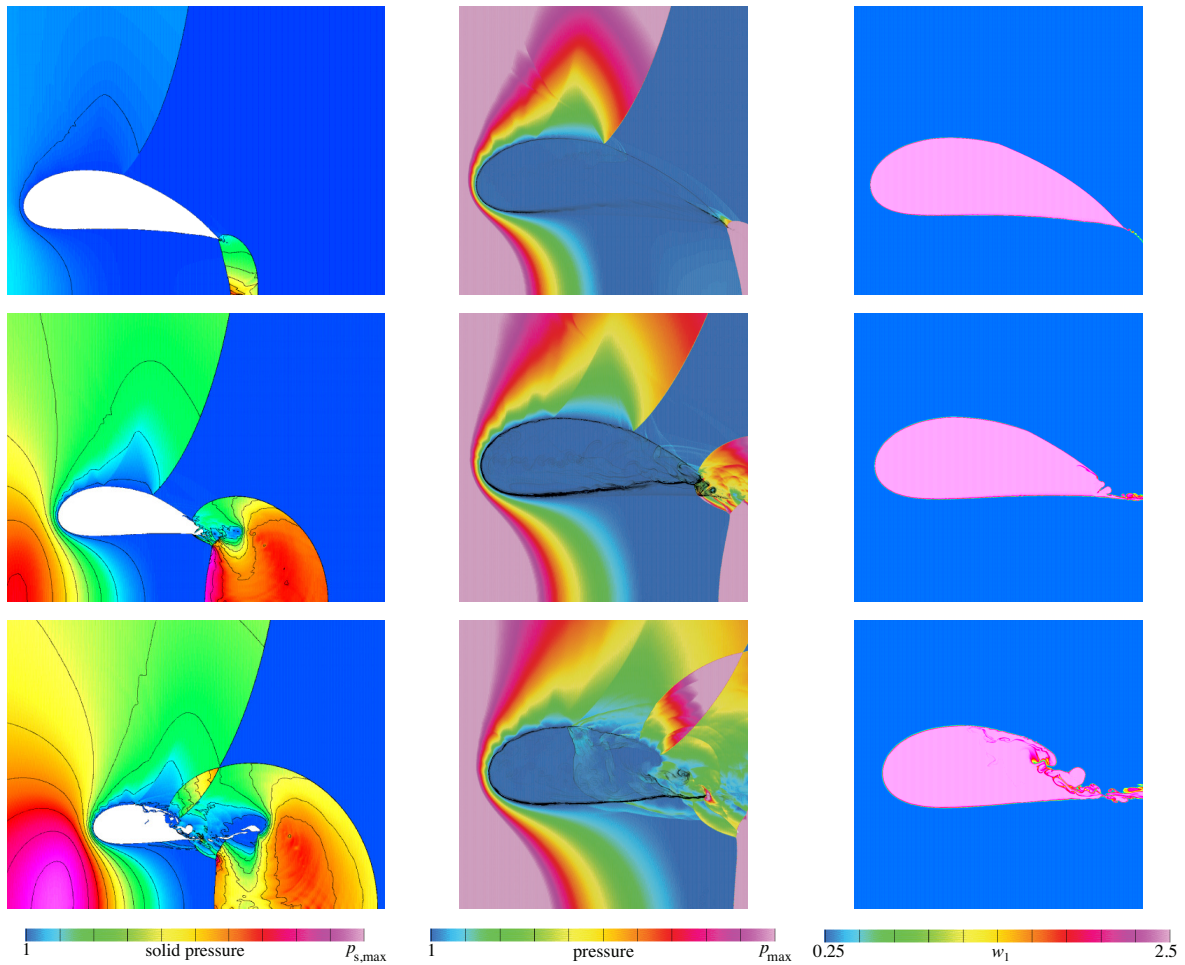
Fig. 25 Long cavity, $M_s = 2.0$. Shaded contours of pressure in the solid (left), enlarged views of pressure in the solid and gas (middle) and w_1 (right) for shock-induced cavity collapse at times $t = 0.090$ (top row: panel (a)), $t = 0.096$ (middle row: panel (b)) and $t = 0.102$ (bottom row: panel (c)). Color bars indicate the range of contours with $(p_{s,max}, p_{max}) = (435000, 20000)$, $(87500, 25000)$ and $(74700, 30000)$ for panels (a), (b) and (c), respectively. The middle-column views show regions of pink color in the high-pressure region ahead of the cavity and in the blast region below the cavity. In these two regions, the pressure is higher than the maximum value for the color range chosen for the plot and thus the color table is saturated there.

ity. The pressure peak on the axis, the extent of the rarefaction region, and the velocity of the jet, all continue to grow. Two new kinks have appeared in the transmitted shock, the secondary discontinuities associated with the original kink have suffered reflections at the cavity wall, and the slip line has begun to roll up. At $t = 0.072$, panel (c), the flow outside the cavity, while having gained strength in such aspects as the velocity of the jet and the size of the on-axis pressure peak, remains unaltered qualitatively. Within the cavity the transmitted shock persists as the primary structure and is now composed of a curved lower segment, a nearly vertical middle segment and a straight upper segment that anchors the structure to the incident shock. Behind the transmitted shock the flow has now become significantly more complex, as kinks in the primary shock have given birth to additional structures, existing slip lines have experienced increasingly prominent rollups, and discontinuities have undergone mul-

tiple interactions among themselves and reflections off the cavity wall. The complexity within the cavity only grows with further deformation of the cavity, and at $t = 0.084$, panel (d), we see a strongly involuted cavity whose dimension along the principal axis has been reduced to less that 8% of its original size. The on-axis behavior thus far of pressure and axial velocity is captured in the profiles displayed in Figure 24. We take note of the acceleration of the jet and the temporal rise in the pressure maximum which, at about 1.5 times the initial post-shock value, is now much higher than was the case at the corresponding stage for the spherical cavity; see Figure 20.

The second state of evolution commences at $t = 0.090$ (Figure 25) when the jet has forced the front face of the cavity to crash into the rear face, thereby initiating the collapse of the cavity and, as in the spherical configuration discussed earlier, generating an expanding region of highly pressur-
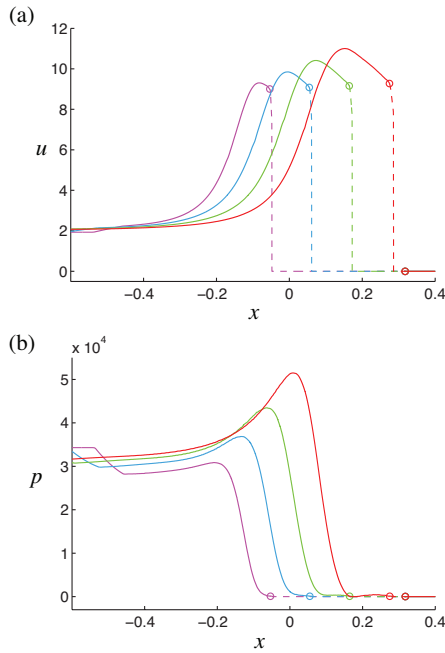
Fig. 24 Long cavity, $M_s = 2.0$. Profiles of (a) axial velocity u and (b) pressure p along the axis of symmetry at $t = 0.048, 0.060, 0.072$ and 0.084. The interface is marked by an open circle. Solid curves indicate the behavior of the solid while dashed curves show the behavior of the gas.

Fig. 26 Long cavity, $M_s = 2.0$. Profiles of (a) axial velocity u and (b) pressure p in the solid along the axis of symmetry at $t = 0.090, 0.096$ and 0.102.

ized solid confined by two blast waves traveling in opposite directions. The events at this stage are visualized, as in earlier cases, in the formats already used in Figures 15 and 21. Three different time levels are considered. At $t = 0.090$ the highest pressure within the blast is on axis immediately behind the left-traveling shock, as can be seen in the left image of panel (a). The w_1 plot in that panel demonstrates the splitting of the cavity subsequent to collapse, and the pressure plot in the middle image shows that the transmitted shock, having reflected from the upper face of the cavity, has sent a weak pressure disturbance into the solid. In the wedge-shaped tail of the cavity the repeated shock reflections have generated a region of elevated pressure, and consequent pressure waves into the solid, as before. At $t = 0.096$, panel (b), the cavity has shrunk while the blast has expanded to cover a broader region, much of the breadth being attributable to the rightward-traveling shock advancing rapidly into a stationary region of low pressure. As noted in earlier cases, the leftward-traveling shock does not make as much headway as its advance is hindered by the rapid rightward-moving jet. Both shock waves have lost strength. The plot of w_1 displays a hint of solid intrusion into the cavity. Finally, at $t = 0.102$, panel (c), the rightward-traveling shock has met and interacted with the incident shock as the latter has progressed down the upper face of the cavity. The collision of the two shocks has generated a domain of localized high pressure. The w_1 plot does show an increased
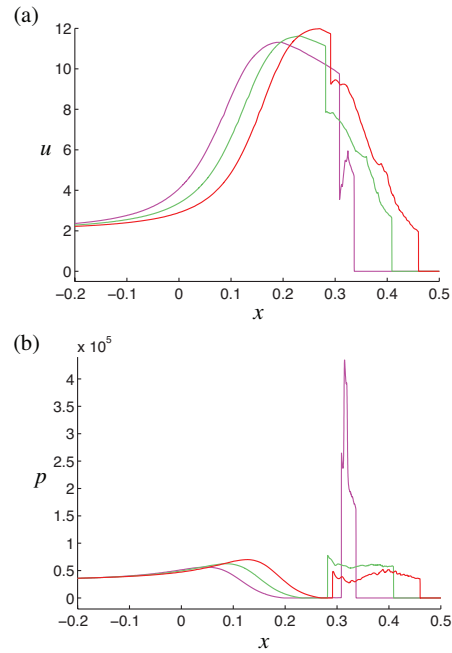
infiltration of the cavity by the high-pressure solid, but the narrow jet resulting therefrom does not lead to any pressure pulses of significant strength transmitted from the cavity into the solid, contrary to what was seen for the spherical cavity.

The on-axis plots of pressure and axial velocity at these later times are shown in Figure 26. The pressure plot shows that the peak of the blast, at $t = 0.090$, is now much higher than the corresponding value for the spherical case (Figure 20). At 435000 it is now more than 12 times the initial postshock value. We note in particular that as the blast spreads and decays, the pressure bump ahead of the cavity still continues to build up, and at the last time shown, $t = 0.102$, the highest pressure on axis is not within the blast but rather at the pressure bump, only marginally above the initial postshock value.

5.4 Tall cavity (oblate spheroid): $M_s = 2.0$

As a final case, we examine the response of an ellipsoidal cavity in the shape of an oblate spheroid, with the major axis again twice as long as the minor axis, and the volume equal to that of the sphere considered earlier. The Mach number of the incident shock remains at the value, $M_s = 2.0$, of the previous two cases.

Figure 27 shows the early stage of the evolutionary process at three times. We begin at $t = 0.040$, panel (a), when the incident shock has gone past the apex of the cavity. The front wall of the cavity shows evidence of folding in, but
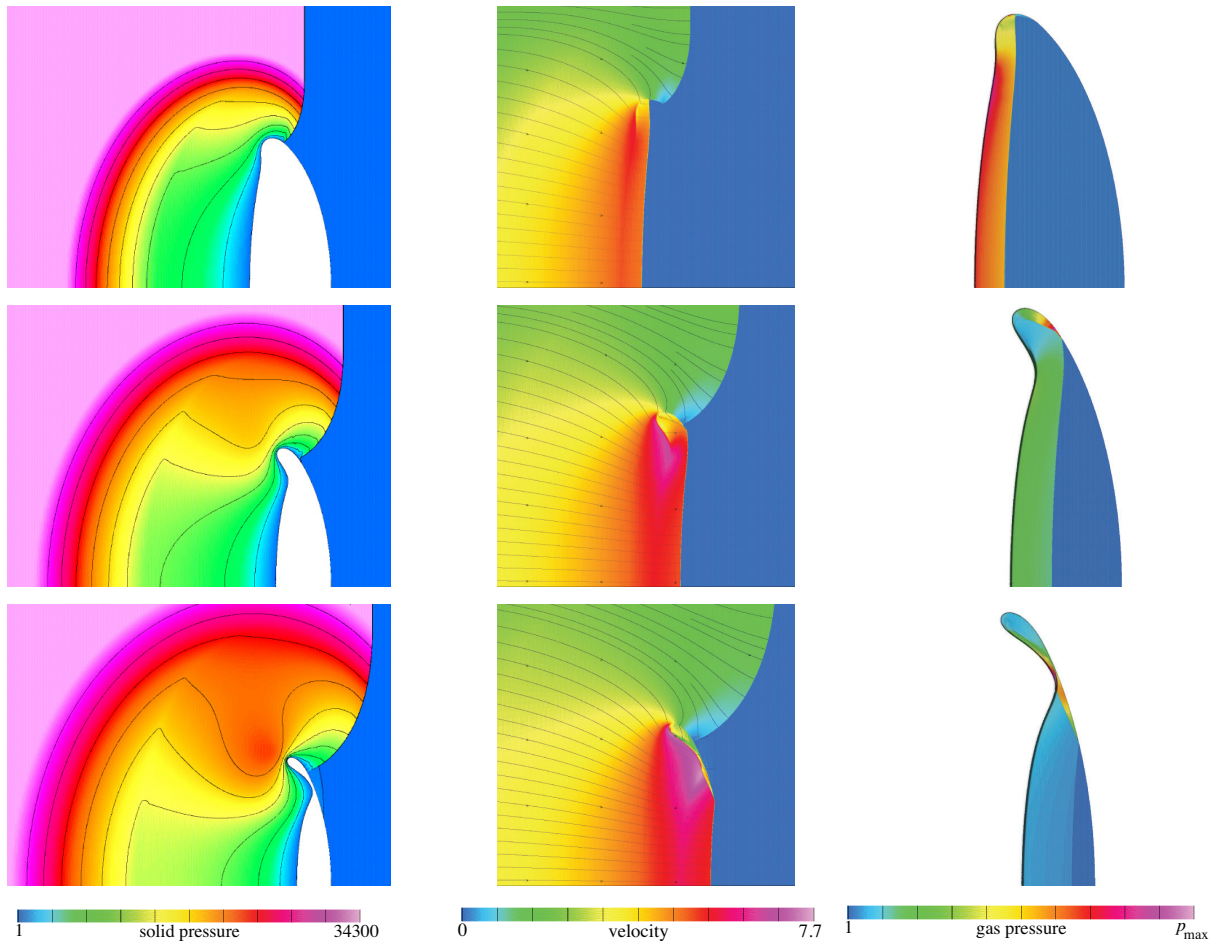
Fig. 27 Tall cavity, $M_s = 2.0$. Shaded contours of pressure in the solid (left), magnitude of velocity (middle) and pressure in the gas (right) for shock-induced cavity collapse at times $t = 0.040$ (top row: panel (a)), $t = 0.048$ (middle row: panel (b)) and $t = 0.054$ (bottom row: panel (c)). Color bars indicate the range of contours with $p_{max} = 74$, 330 and 1600 for panels (a), (b) and (c), respectively. The images of the magnitude of velocity and pressure in the gas are enlarged.

only at the off-axis location near the top of the cavity. One is also struck by the fact that the rarefaction is rather weak compared to that in the configurations discussed earlier, and consequently, so is the convergence of the flow and the strength of the jet. Within the cavity the reflected shock is nearly parallel to the front face of the cavity, with just a hint of a transverse arm at the top forming the gamma shape. At $t = 0.048$, panel (b), the cavity continues to involute, and within it the upper portion of the transmitted shock has undergone reflection from the rear wall of the cavity. At $t = 0.054$, panel (c), a local pressure bump is visible just upstream of the apex of the cavity. The front wall of the cavity is just about to collide with the rear wall, thereby launching the process of cavity collapse. Collapse is now initiated off-axis, and results in the separation of a small lobe from the main body of the cavity. We note from the solid pressure color bar for the first column that at this stage the off-axis pressure peak immediately ahead of the cavity is far below the initial post-shock value of $\tilde{p}_s = 34300$.

The next stage of evolution is displayed in Figure 28 at three different instants of time. The overall pressure in the solid is displayed in the left image, an expanded view of the pressure within and around the upper lobe of the cavity in the middle image, and an expanded view of the pressure within and around the lower lobe of the cavity in the middle image. At $t = 0.056$ the collapse has led to an expanding high-pressure blast region between the two lobes. Within this region pressure is highest at the bottom and lowest at the top. Within the upper lobe we see the by-now familiar gasdynamic structures consisting of criss-crossing shocks and rolled-up slip lines, with pressure higher in the wedge-shaped lower portion. In the lower lobe the wedge-shaped upper portion exhibits a similar pattern of reflecting shocks. At $t = 0.058$ the right-traveling shock bounding the blast region has collided with the incident shock, but the latter is too weak to result in significant local pressure rise. The upper lobe continues to shrink, and pressure disturbances due to the high pressure within are being transmitted into the solid
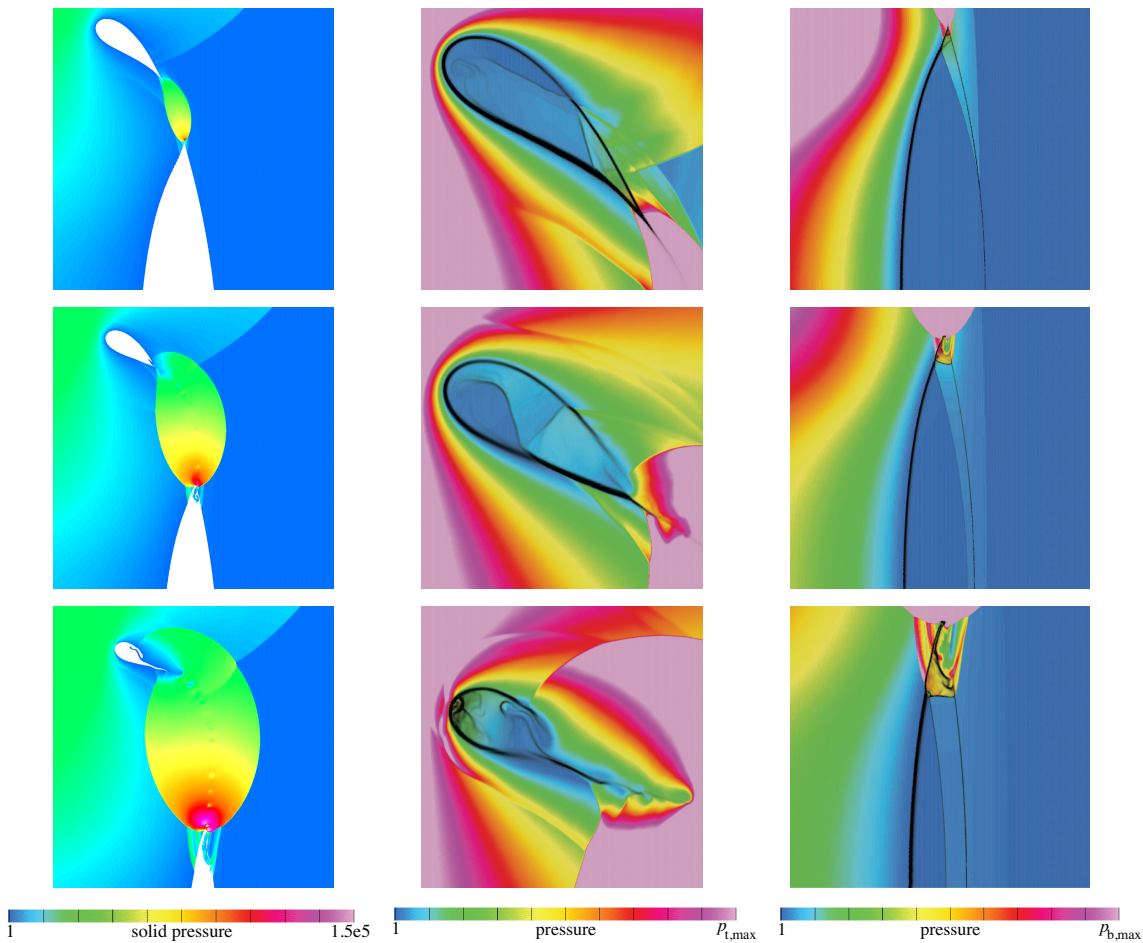
Fig. 28 Tall cavity, $M_s = 2.0$. Shaded contours of pressure in the solid (left), and enlarged views of pressure in the solid and gas (middle and right) for shock-induced cavity collapse at times $t = 0.056$ (top row: panel (a)), $t = 0.058$ (middle row: panel (b)) and $t = 0.060$ (bottom row: panel (c)). Color bars indicate the range of contours with $(p_{t,max}, p_{b,max}) = (10000, 10000)$, $(15000, 20000)$ and $(20000, 30000)$ for panels (a), (b) and (c), respectively. The middle and right-column views show regions of pink color in the high-pressure region ahead of the cavity and in the blast region adjacent to the cavity. In these regions, the pressure is higher than the maximum value for the color range chosen for the plot and thus the color table is saturated there.

surrounding the lobe. Some solid has penetrated the upper portion of the lower lobe, and as in earlier cases, discrete pressure peaks have begun to emanate into the surrounding solid. These processes continue at $t = 0.060$, and one can now see the evidence of some solid infiltration into the upper lobe as well. We note that pressures within the lower lobe are higher than those in the upper lobe. Furthermore, the color bar indicates the pressure peak within the blast is about four times the initial post-shock value at this time.

The final stage of evolution is shown in Figure 29. With the upper lobe having shrunk substantially in size, attention is focused on the events in the lower lobe, and pressure plots are shown at three different times. As the lead shock front in the lobe and the slender solid jet hugging the rear wall of the lobe advance downwards, additional pressure pulses are transmitted into the surrounding solid, as seen at $t = 0.061$ and $t = 0.062$. At $t = 0.063$, the lead disturbance within the

lobe has reflected off the axis, thereby generating a local region of exceedingly high pressure, close to thirty times the initial post-shock value.

6 Conclusions

The flow field resulting from the interaction between a planar incident shock in the solid and an embedded ellipsoidal gas cavity has been examined computationally. We have employed a Godunov type, adaptive numerical scheme of high resolution that treats the two immiscible components as a mixture, recognizing that in practical terms both components coexist only within a very thin interface. Such a scheme obviates the need for a special treatment of the interface, which is captured as the computation proceeds. The focus has been on the pressure field generated within the solid as a result of the incident solid shock interacting with the gas
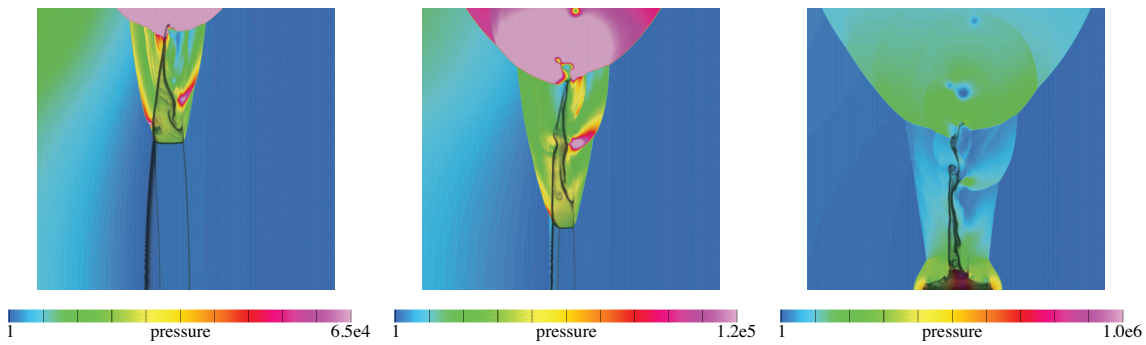
Fig. 29 Tall cavity, $M_s = 2.0$. Shaded contours of pressure for shock-induced cavity collapse at times $t = 0.061$ (left), $t = 0.062$ (middle) and $t = 0.063$ (right).

cavity, and in particular on the magnitude of the pressure peaks and the extent and location of the regions in which pressure levels above the initial post-shock value are generated. We have examined four different cases corresponding to two different incident Mach numbers, $M_s = 1.2$ and 2.0, and three different cavity shapes, spherical, prolate spheroid (long) and oblate spheroid (tall). Significant attention has been given to illustrate the process of cavity collapse in terms of highly-resolved plots of pressure, velocity, and the waves produced in the flow. These plots also provided a quantitative description of the collapse and of the peak pressures generated.

The accuracy of the calculations has been assessed by examining the results of several test flow configurations and by grid refinement studies of the results of the collapse of a spherical cavity for the case of an incident shock with $M_s = 1.2$. These calculations indicate that the fine-grid solutions accurately capture the behavior of the interface, shocks in both the solid and gas, and in particular the collapse of the cavity and the resulting blast waves. It has been noted that some fine-scale features of the late-time behavior of the flow in the vicinity of the collapsed gas cavity are obtained qualitatively.

We find that in all cases the impact of the shock drives a transmitted shock into the cavity and a rarefaction back into the solid. The rarefaction sets up an oblique pressure gradient that causes the flow approaching the cavity to converge, thus establishing a rapidly moving jet in which the velocity substantially exceeds the initial post-shock value. As the flow evolves, a local pressure maximum appears within the rarefaction. This pressure peak appears on axis for the spherical cavity and for the long cavity, but off-axis for the tall cavity. The jet pushes the front face of the cavity against the rear face, causing the cavity to collapse and giving birth to a pair of oppositely directed blast waves that contain an expanding region of high pressure. The blast region is symmetric with respect to the axis for the spherical cavity and the long cavity, but is located off-axis for the tall cavity. Although the pressure within the blast is relieved as time pro-

ceeds, it remains higher than the initial post-shock pressure for a substantial period. As the cavity continues to shrink, it is infiltrated by a slender jet of high-pressure solid which meanders through the cavity and suffers multiple collisions with the cavity wall, thereby transmitting bursts of high-pressure disturbances into the surrounding solid. Additional regions of elevated pressure develop due to the interaction of the expanding blast region with the incident shock.

We have examined the spherical cavity for $M_s = 1.2$ and 2.0. In both cases the general trends of behavior are similar. While the peak pressures generated within the solid are higher in absolute terms for the higher Mach number case, they are lower when referred to the pre-impact post-shock pressure. The cavity shape also exerts a substantial influence on both the magnitude and the location of the peak pressure. In contrast to the spherical case, one finds that for the long cavity, a higher relative peak pressure is generated ahead of the cavity prior to collapse, as also within the blast region subsequent to collapse. The highest of all peaks, however, is generated for the tall cavity when the shocks moving radially inwards within the lower lobe collide with the symmetry axis.

To the extent that a comparison is possible, our results are in accord with those of earlier numerical studies but extend them in multiple ways. Thus the results for the spherical cavity, $M_s = 2.0$, can be compared with those of Ball *et al.* [4] who considered a similar setup for a cylindrical air cavity immersed in water and subject to impact by an $M_s = 1.9$ shock. While the general evolutionary trends agree, we provide additional details of the on-axis behavior of velocity and pressure, as well as of the post-impact developments within the cavity. The infiltration of the slender solid jet into the gas and the pressure bursts resulting therefrom have not been seen before. The results for the non-spherical cavities are entirely new.

References

1. Abgrall, R.: How to prevent pressure oscillations in mulicomponent flow calculations: A quasi conservative approach. J. Comput. Phys. **125**, 150–160 (1996)

2. Abgrall, R., Karni, S.: Computations of compressible multifluids. J. Comput. Phys. **169**, 594–623 (2001)

3. Arnett, W.: The role of mixing in astrophysics. Astrophys. J. Suppl. Series. **127**, 213–217 (2000)

4. Ball, G.J., Howell, B.P., Leighton, T.G., Schofield, M.J.: Shock-induced collapse of a cylindrical air cavity in water: a free-Lagrange simulation. Shock Waves **10**, 265–276 (2000)

5. Banks, J.B., Schwendeman, D.W., Kapila, A.K., Henshaw, W.D.: A high-resolution Godunov method for multi-material flows on overlapping grids. J. Comput. Physics **223**, 262–297 (2007)

6. Banks, J.B., Schwendeman, D.W., Kapila, A.K., Henshaw, W.D.: A study of detonation propagation and diffraction with compliant confinement. Combust. Theory Modeling **12**, 769–808 (2008)

7. Bourne, N.K.: On the collapse of cavities. Shock Waves **11**, 447–455 (2002)

8. Bourne, N.K., Field, J.E.: Explosive ignition by the collapse of cavities. Proc. R. Soc. Lond. A **455**, 2411–2426 (1999)

9. Chesshire, G., Henshaw, W.: Composite overlapping meshes for the solution of partial differential equations. J. Comp. Phys. **90**, 1–64 (1990)

10. Fickett, W., Davis, W.C.: Detonation. University of California Press, Berkeley (1979)

11. Haas, J.F., Sturtevant, B.: Interaction of weak shock waves with cylindrical and spherical gas inhomogeneities. J. Fluid Mech. **181**, 41–76 (1987)

12. Henshaw, W.D., Schwendeman, D.W.: An adaptive numerical scheme for high-speed reactive flow on overlapping grids. J. Comput. Phys. **191**(2), 420–447 (2003)

13. Henshaw, W.D., Schwendeman, D.W.: Parallel computation of three-dimensional flows using overlapping grids with adaptive mesh refinement. J. Comput. Phys. **227**, 7469–7502 (2008)

14. Jenny, P., Müller, B., Thomann, H.: Correction of conservative Euler solvers for gas mixtures. J. Comput. Phys. **132**, 91–107 (1997)

15. Johnsen, E., Colonius, T.: Shock-induced collapse of a gas bubble in shockwave lithotripsy. J. Acoust. Soc. Am. **124**, 2011–2020 (2008)

16. Khokhlov, A.M., Oran, E.S., Thomas, G.O.: Numerical simulation of deflagration-to-detonation transition: the role of shock-flame interaction in turbulent flames. Comb. Flame **117**, 323–329 (1999)

17. Marble, F.E., Hendricks, G.J., Zuboski, E.E.: Progress toward shock enhancement of supersonic combustion processes. AIAA J. **87**, 87–97 (1989)

18. Milne, A., Bourne, N.: Experimental and numerical study of temperature in cavity collapse. In: N.T. M.D. Furnish, Y. Horie (eds.) Shock Compression of Condensed Matter, vol. CP620, pp. 131–176. American Institute of Physics (2002)

19. Quirk, J.J., Karni, S.: On the dynamics of a shock-bubble interaction. J. Fluid Mech. **318**, 129–163 (1996)

20. Roache, P.J.: Code verification by the method of manufactured solutions. J. Fluids Eng. **124**, 4–10 (2002)

21. Roy, C.J., Nelson, C.C., Smith, T.M., Ober, C.C.: Verification of Euler/Navier-Stokes codes using the method of manufactured solutions. Int. J. Numerical Methods Fluids **44**, 599–620 (2004)

22. Saurel, R., Abgrall, R.: A simple method for compressible multifluid flows. SIAM J. Sci. Comput. **21**(3), 1115–1145 (1999)

23. Schwendeman, D.W., Kapila, A.K., Henshaw, W.D.: A study of detonation diffraction and failure for a model of compressible two-phase reactive flow. Combust. Theory and Modeling **14**, 331–266 (2010)

24. Schwendeman, D.W., Wahle, C.W., Kapila, A.K.: The Riemann problem and a high-resolution Godunov method for a model of compressible two-phase flow. J. Comput. Phys. **212**, 490–526 (2006)

25. Toro, E.F.: Riemann Solvers and Numerical Methods for Fluid Dynamics. Springer, Berlin (1999)

26. Whitham, G.B.: Linear and Nonlinear Waves. Wiley-Interscience, New York (1974)

27. Zhang, Q., Graham, M.: A numerical study of richtmeyer instability driven by cylindrical shocks. Phys. Fluids **10**, 974–993 (1998)